

Evolution of thermal and nonthermal radio continuum emission on kpc scales—Predictions for SKA

M. Ghasemi-Nodehi¹, Fatemeh S. Tabatabaei^{1,2,3*}, Mark Sargent^{4,5}, Eric J. Murphy⁶,

Habib Khosroshahi¹, Rob Beswick⁷, Anna Bonaldi⁸, Eva Schinnerer³

¹*School of Astronomy, Institute for Research in Fundamental Sciences, 19395-5531, Tehran, Iran*

²*Instituto de Astrofísica de Canarias, E-38205 La Laguna, Tenerife, Spain*

³*Max-Planck-Institut für Astronomie, Königstuhl 17, D-69117 Heidelberg, Germany*

⁴*International Space Science Institute (ISSI), Hallerstrasse 6, CH-3012 Bern, Switzerland*

⁵*Astronomy Centre, Department of Physics & Astronomy, University of Sussex, Brighton, BN1 9QH, England*

⁶*National Radio Astronomy Observatory, 520 Edgemont Road, Charlottesville, VA 22903, USA*

⁷*Jodrell Bank Centre for Astrophysics/e-MERLIN, The University of Manchester, M13 9PL, UK*

⁸*SKA Organisation, Jodrell Bank, Lower Withington, Macclesfield, Cheshire SK11 9FT, UK*

Accepted XXX. Received YYY; in original form ZZZ

ABSTRACT

Resolved maps of the thermal and nonthermal radio continuum (RC) emission of distant galaxies are a powerful tool for understanding the role of the interstellar medium (ISM) in the evolution of galaxies. We simulate the RC surface brightness of present-day star forming galaxies in the past at $0.15 < z < 3$ considering two cases of radio size evolution: (1) no evolution, and (2) same evolution as in the optical. We aim to investigate the a) structure of the thermal and nonthermal emission on kpc scales, b) evolution of the thermal fraction and synchrotron spectrum at mid-radio frequencies ($\simeq 1\text{--}10$ GHz), and c) capability of the proposed SKA1-MID reference surveys in detecting the RC emitting structures. The synchrotron spectrum flattens with z causing curvature in the observed mid-radio SEDs of galaxies at higher z . The spectral index reported in recent observational studies agrees better with the no size evolution scenario. In this case, the mean thermal fraction observed at 1.4 GHz increases with redshift by more than 30% from $z = 0.15$ to $z = 2$ because of the drop of the synchrotron emission at higher rest-frame frequencies. More massive galaxies have lower thermal fractions and experience a faster flattening of the nonthermal spectrum. The proposed SKA1-MID band 2 reference survey, unveils the ISM in M51- and NGC6946-like galaxies (with $M_\star \simeq 10^{10} M_\odot$) up to $z = 3$. This survey detects lower-mass galaxies like M33 ($M_\star \simeq 10^9 M_\odot$) only at low redshifts $z \lesssim 0.5$. For a proper separation of the RC emitting processes at the peak of star formation, it is vital to include band 1 into the SKA1-MID reference surveys.

Key words: Radio Continuum: Galaxies, Galaxies: ISM, Galaxies: Star Formation, Galaxies: Evolution

1 INTRODUCTION

The interstellar and intergalactic media play an important role in galaxy formation and evolution as they host the cool gas reservoir needed to form stars and fuel supermassive black hole accretion (e.g. Daddi et al. 2010; Greve et al. 2005; Tacconi et al. 2013; Walter et al. 2016, 2020; Zovaro et al. 2022). Galaxies experience star formation quenching over cosmic time that is linked to a lack of cool gas caused by different mechanisms such as feedback and starvation (e.g. Schaye et al. 2015; Gatto et al. 2002; Peng et al. 2015). However, ample amounts of cool gas can be found in quenched systems which are, for an unknown reason, inefficient in forming massive stars (Brownson et al. 2020; Hunt et al. 1935; Scoville et al. 2017; Tacconi et al. 2018). Thus, factors con-

trolling gas against collapse and accretion over cosmic time must be better understood. Observations show that nonthermal pressures inserted by cosmic rays and magnetic fields can be more significant than the thermal gas pressure in nearby galaxies (Beck 2007; Tabatabaei et al. 2008; Hassani et al. 2021). The nonthermal processes can support cool gas against accretion from the IGM (Grϕnnow et al. 2022; Mathews 2009; Owen et al. 2013) and collapse/fragmentation in the ISM (e.g., Pillai et al. 2015; Tabatabaei et al. 2018) decreasing the star formation rate (SFR). Therefore, it is very insightful to dissect the thermal and nonthermal processes over cosmic time. These processes can be very well studied through mapping the radio continuum (RC) emission in galaxies. The thermal free-free emission and the nonthermal synchrotron emission, the two main components of the RC emission, emerge from the thermal ionized gas and the nonthermal magnetized/relativistic ISM, respectively. The

* Corresponding author E-mail: ftaba@ipm.ir

power-law index of the nonthermal synchrotron spectrum, that is related to the energy index of cosmic ray electrons, changes with location in a galaxy, being flatter in star-forming regions and steeper in inter-arm regions and outer disks (Tabatabaei et al. 2007b, 2013a; Hassani et al. 2021). This indicates that cosmic rays are more energetic closer to their birthplace in star-forming regions (e.g., in supernova remnants) than in other media due to cooling mechanisms (e.g., Longair 1994). Global surveys such as KINGFISH (Key Insights on Nearby Galaxies; a Far-Infrared Survey with Herschel, Kennicutt et al. 2011) also find that the nonthermal spectrum in galaxies with higher star formation rate surface density is flatter. This shows that the bulk of the cosmic ray electron population is younger and more energetic due to massive star formation activities (Tabatabaei et al. 2017). Combined with polarization observations, the synchrotron emission reveals that the turbulent magnetic field becomes stronger with star formation rate as shown in both local and global studies (Niklas & Beck 1997; Chyży, et al. 2011; Heesen et al. 2014). Strong turbulent magnetic fields and a large number of high energy particles can cause strong winds and outflows in starbursting galaxies. This implies an important role of magnetic fields and cosmic rays in driving so called 'feedback' in galaxies (Pfrommer et al. 2017).

Deep and resolved RC observations at high-redshifts are needed to address the exact role of the thermal and nonthermal processes and the origin of feedback. Currently available radio deep field surveys have, however, too low angular resolution and sensitivity to allow for separation of the thermal and nonthermal emission in distant galaxies. The advent of the Square Kilometer Array (SKA) and its instrumental capabilities combined with ground-breaking results from ALMA, VLT/MUSE (and others) which trace different phases of the gaseous ISM will shed light on this subject.

The RC emission from star-forming galaxies has been often used as an extinction-free tracer of star formation rate (SFR) at all redshifts mainly because of its tight correlation with the infrared (IR) emission (see e.g., Condon et al. 2002; Gran et al. 2009; Garrett 2002; Appleton et al. 2004; Sajina et al. 2008; Sargent et al. 2010; Leslie et al. 2020, and references therein). However, there are works questioning the RC–IR's direct connection to star formation suggesting a conspiracy of several factors (e.g. Bell 2003; Lacki et al. 2010). Moreover, several studies show that the RC–IR correlation can deviate from linearity at high- z (e.g., Magnelli et al. 2015; Basu et al. 2015; Delhaize et al. 2017) and in nearby galaxies (e.g. Niklas & Beck 1997; Dumas et al. 2011; Heesen et al. 2014) depending on galaxy mass and type (e.g. Delvecchio et al. 2017; Read et al. 2018; Molnar et al. 2021) and the ISM conditions and spatial scale (e.g. Tabatabaei et al. 2013a,b). The non-linearity of the global correlation occurs mainly at high SFRs (Tabatabaei et al. 2017) and this can be observed with redshift as the SFR increases with redshift (e.g., Molnar et al. 2021).

Murphy et al. (2011) presented the RC–SFR calibration relations for both the thermal and nonthermal emission which are independent from the RC–IR correlation and show that, in the HII complexes of NGC6946, the thermal RC emission provides a more robust SFR tracer as it can be directly linked to the ionizing photon rate arising from newly formed massive stars. Using the same physically motivated relations and separating the thermal and nonthermal RC emission through

a detailed study of the mid-radio (1-10 GHz) spectral energy distribution (SED), Tabatabaei et al. (2017) showed that, on galaxy scales, the standard non-radio SFR tracers hold a tighter correlation with the nonthermal RC than with the thermal RC, although the linearity is better achieved with the thermal emission. These authors link the non-linearity, i.e. the excess of the nonthermal emission, to a stronger magnetic field in galaxies with higher SFR.

In this paper, we study the cosmic evolution of the thermal and nonthermal RC emission from star-forming galaxies taking into account the evolution of SFR and using the thermal/nonthermal RC–SFR correlations (given by Murphy et al. 2011; Tabatabaei et al. 2017). The most fundamental questions are if the thermal fraction of the RC emission remains invariant with redshift and how the nonthermal spectrum at mid-radio frequencies of $\simeq 1-10$ GHz evolve with cosmic time. We perform simulations to investigate the detectability of the ISM structures by the proposed SKA surveys. The Galaxies selected are like those in the local universe as if they were at higher redshifts. Comparing these predictions with the upcoming real SKA observations will further help to infer any difference in the ISM properties of galaxies in the distant universe. The goals of this study are then to investigate 1) the structure of the thermal and nonthermal emission on 1 kpc scales at different redshifts, 2) possible evolution of the thermal fraction and the mid-radio synchrotron spectral index, and 3) the capability of the proposed SKA reference surveys to detect the RC emitting structures, which is important to address the role of the thermal/nonthermal processes in the evolution of galaxies.

Separating the thermal and nonthermal components of the RC emission has historically been a technical challenge. It basically needs multi-frequency radio observations with proper frequency sampling and consistent sensitivities at different frequencies. Insufficient frequency coverage requires pre-assumptions about the nonthermal spectral index (e.g., Klein et al. 1984). Moreover, because the sensitivity changes naturally with frequency, available separations are limited to only a few bright sources or very coarse angular resolutions in nearby galaxies (e.g., Westcott et al. 2018). We developed a separation technique for nearby galaxies that is based on a tracer of the free-free emission, like a de-reddened $H\alpha$ map (Tabatabaei et al. 2007b, 2013a,b). This method can separate the thermal and nonthermal components down to very low surface brightnesses enabling us to study different galactic structures. The present study uses the results of this separation method applied to local galaxies as initial inputs to further investigate the ability of the SKA to detect such structures at higher redshifts.

The paper is organized as follows. After presenting the theoretical framework, we explain the different steps taken to construct simulated maps in section 2. The resulting maps of the thermal and nonthermal RC emission and their redshift profiles are presented in Sect 3. We further discuss the evolution of synchrotron spectral indices, the spectral energy distribution, and the compatibility with the SKA surveys in Sect. 4 and summarize in Sect. 5.

2 METHODOLOGY

Deep field observations show that galaxies' SFRs evolve

with redshift z depending on the stellar mass of galaxies. We first review this SFR evolution and then obtain relations for the evolution of the thermal and nonthermal RC emission. These relations are then used to simulate the RC maps of three prototypical galaxies as observed by SKA. We use $H_0 = 67.4$ km/s/Mpc, $\Omega_m = 0.31$, and $\Omega_\Lambda = 0.68$ (Planck Collaboration et al. 2018) throughout the paper.

2.1 Evolution of star formation rate

Evolution of SFR has been the topic of several observational studies (e.g., Seymour et al. 2008; Driver et al. 2013; Madau & Dickinson 2014; Speagle et al. 2014; Scoville et al. 2016). Star-forming galaxies follow a tight SFR–stellar mass (M_*) correlation, with a dispersion of about 0.3 dex forming the so called *main sequence* (MS) of galaxies in the SFR– M_* plane (Noeske et al. 2007). Although the log-log slope of this correlation and its normalization can depend on galaxy sample and the SFR tracer (e.g., Speagle et al. 2014; Bisigello et al., 2018; Leslie et al. 2020), a large number of studies find strong evolution out to at least $z = 4$ with a roughly linear relation at low masses and an increasing tendency for bending or flattening at high mass and lower redshift (e.g., Whitaker et al. 2014; Lee et al. 2015; Schreiber et al. 2015; Tomczak 2016; Leslie et al. 2020). A well-presented parametrization of the SFR evolution of the MS galaxies, including all the aforementioned features, was introduced by Schreiber et al. (2015). This was performed by combining deep far-infrared data taken with the Herschel Space Observatory with the UV to near-infrared data of four major extragalactic fields GOODS-North, GOODS-South, UDS, and COSMOS for a mass complete sample of star-forming galaxies. They found that the SFR of galaxies of all stellar masses (M_*) at $z \leq 4$ follow a universal scaling law showing a close-to-linear slope of the $\log(\text{SFR})$ - $\log(M_*)$ relation:

$$\log_{10}(\text{SFR}_{\text{MS}}[\text{M}_\odot\text{yr}^{-1}]) = m - m_0 + a_0 r \quad (1)$$

$$- a_1 [\max(0, m - m_1 - a_2 r)]^2$$

with $r \equiv \log(1 + z)$ and $m \equiv \log(M_*/10^9\text{M}_\odot)$. Other parameters in the above relation are $m_0 = 0.5 \pm 0.07$, $a_0 = 1.5 \pm 0.15$, $a_1 = 0.3 \pm 0.08$, $m_1 = 0.36 \pm 0.3$, and $a_2 = 2.5 \pm 0.6$. Dispersion in this relation is reportedly about 0.3 dex, i.e., at a fixed redshift and stellar mass, about 68% of star-forming galaxies form stars at a universal rate within a factor 2 (Schreiber et al. 2015).

2.2 Evolution of thermal and nonthermal emission

The RC emission is often described by a power-law function of frequency ν , $S_\nu \propto \nu^{-\alpha}$, with S_ν the integrated flux density and α the power-law spectral index. It originates mainly from two different emission mechanisms, the nonthermal synchrotron emission and the thermal free-free emission, $S_\nu = S_\nu^{\text{th}} + S_\nu^{\text{nt}}$. The nonthermal and thermal emission are also power-law functions of ν with different spectral indices α_{nt} and α_{th} , respectively: $S_\nu^{\text{nt}} \propto \nu^{-\alpha_{\text{nt}}}$ and $S_\nu^{\text{th}} \propto \nu^{-\alpha_{\text{th}}}$. For a galaxy at redshift $z \sim 0$ the relation between the integrated flux density and luminosity is: $L_\nu = S_\nu 4\pi D^2$, with

D the distance, while at high redshifts, taking into account the k-correction of $K(z) = (1+z)^{-(1-\alpha)}$, we get¹

$$L_{\nu_1} = \frac{4\pi D_L^2(z)}{(1+z)^{1-\alpha}} \left(\frac{\nu_1}{\nu_2}\right)^{-\alpha} S_{\nu_2}, \quad (2)$$

where L_{ν_1} is the radio luminosity at rest-frame frequency ν_1 and S_{ν_2} is the integrated flux density observed at frequency ν_2 and $D_L(z)$ is the luminosity distance at redshift z .

Murphy et al. (2011) obtained the following calibration relations between the SFR and the thermal and nonthermal radio luminosities, L_ν^{th} and L_ν^{nt} , using a Kroupa IMF (Kroupa 2002) and assuming a solar metallicity and continuous star formation over a timescale of ~ 100 Myr ,

$$\left(\frac{\text{SFR}_{\nu_1}^{\text{th}}}{\text{M}_\odot\text{yr}^{-1}}\right) = 4.6 \times 10^{-28} \left(\frac{T_e}{10^4\text{K}}\right)^{-0.45} \quad (3)$$

$$\times \left(\frac{\nu_1}{\text{GHz}}\right)^{\alpha_{\text{th}}} \left(\frac{L_{\nu_1}^{\text{th}}}{\text{erg s}^{-1}\text{Hz}^{-1}}\right),$$

$$\left(\frac{\text{SFR}_{\nu_1}^{\text{nt}}}{\text{M}_\odot\text{yr}^{-1}}\right) = 6.64 \times 10^{-29} \left(\frac{\nu_1}{\text{GHz}}\right)^{\alpha_{\text{nt}}} \quad (4)$$

$$\times \left(\frac{L_{\nu_1}^{\text{nt}}}{\text{erg s}^{-1}\text{Hz}^{-1}}\right),$$

with T_e the electron temperature. A calibration between the supernova rate and the SFR was applied for Eq. 4 using the empirical relations between supernova rate and nonthermal spectral luminosity of the Milky Way. Hence, S_{ν_2} in Eq. 2 evolves as

$$S_{\nu_2}(z) = S(0) \frac{\text{SFR}_{\nu_1}(z)}{\text{SFR}(0)} \frac{D^2}{D_L^2} (1+z)^{1-\alpha}, \quad (5)$$

with $S(0)$, $\text{SFR}(0)$, and D being the actual integrated flux density, star formation rate, and distance to the $z \sim 0$ local Universe galaxies² used in our simulation ($S(0) = \frac{L_{\nu_1}(0)}{4\pi D^2} \propto \text{SFR}(0)$) following Eq. 3 for the thermal emission and Eq. 4 for the nonthermal emission³.

Similarly, to obtain the evolution of the surface brightness, $I_{\nu_2}(z)$, the evolution of the luminosity density at the rest-frame frequency, ΣL_{ν_1} , must be known,

$$\Sigma L_{\nu_1} = \frac{4\pi D_L^2(z)}{(1+z)^{1-\alpha}} \left(\frac{\nu_1}{\nu_2}\right)^{-\alpha} I_{\nu_2}, \quad (6)$$

The same relations as in Eqs. 3 and 4 hold between ΣL_{ν_1} and the surface density of the star formation rate, $\Sigma \text{SFR}_{\nu_1}$. However, it is not that straightforward to directly link the evolution of $\Sigma \text{SFR}_{\nu_1}$ to that of SFR_{ν_1} . Several deep field optical studies find that the stellar size of galaxies evolves with redshift (e.g., Ferguson et al. 2004; Mosleh et al. 2011; Ono et al. 2013; van der Wel et al. 2014; Shibuya et al. 2015; Suess et al. 2019). These studies also show that the evolution becomes shallower at longer wavelengths. In the radio domain, this subject awaits multi-wavelength observations and it is still under debate (see Sect. 4.3.1). Therefore, accounting for different possibilities, we consider two extreme scenarios:

¹ α is equivalent to α_{nt} for the nonthermal emission and α_{th} for the thermal emission

² Note that the rest-frame frequency is equal to the observed frequency at $z=0$ and $S_{\nu_1}(0) = S_{\nu_2}(0) = S(0)$.

³ It is clear that $\text{SFR}^{\text{th}} = \text{SFR}^{\text{nt}} = \text{SFR}$

Galaxy	D^a Mpc	M_\star^b M_\odot	SFR ^c $M_\odot\text{yr}^{-1}$	SFR(0) ^d $M_\odot\text{yr}^{-1}$	SFR(0.5) ^e $M_\odot\text{yr}^{-1}$	SFR(1) ^f $M_\odot\text{yr}^{-1}$	SFR(2) ^g $M_\odot\text{yr}^{-1}$	SFR(3) ^h $M_\odot\text{yr}^{-1}$	$\alpha_{\text{nt}}(0)^j$
M51	7.60	$10^{10.56}$	3.1	4.2	14.2	28.3	59.7	91.8	0.95 ± 0.09
N6946	6.80	$10^{9.96}$	3.2	2.3	5.2	8.2	15.0	23.1	0.80 ± 0.06
M33	0.84	$10^{9.54}$	0.5	1.1	2.0	3.1	5.7	8.8	0.86 ± 0.08

Table 1. Galaxy sample and their properties. (a) Distance to M51: [Ciardullo et al. \(2002\)](#), NGC6946: [Karachentsev et al. \(2000\)](#), and M33: [Freedman et al. \(1991\)](#). (b) Stellar mass of M51: [Karachentsev et al. \(2013\)](#), NGC6946: [Kennicutt et al. \(2011\)](#), and M33: [Corbelli \(2004\)](#). (c) SFR estimates from literature for M51 & NGC6946: [Leroy et al. \(2008\)](#), M33: [Verley et al. \(2009\)](#). (d)–(h) SFR of the main sequence galaxies with M_\star of M51, NGC6946, and M33 given by Eq. (1) at $z = 0, 0.5, 1, 2$ and 3 respectively. (j) Nonthermal spectral index of M51 & NGC6946: [Tabatabaei et al. \(2017\)](#), and M33: [Berkhuijsen, et al. \(2013\)](#).

(1) The SFR and its surface density evolve similarly with z , i.e.,

$$\frac{\Sigma \text{SFR}(z)}{\Sigma \text{SFR}(0)} = \frac{\text{SFR}(z)}{\text{SFR}(0)}, \quad (7)$$

with SFR(0) and $\Sigma \text{SFR}(0)$ the corresponding rates at $z=0$. In case (2), the surface density of star formation rate changes additionally due to the evolution of the galaxies' effective radii⁴, r_e as $\Sigma \text{SFR} \propto \text{SFR}/r_e^2$. The size evolution of galaxies is given by $r_e \propto (1+z)^{-0.75}$ ([van der Wel et al. 2014](#); [Straatman, et al. 2015](#)), thus for case (2) we obtain

$$\frac{\Sigma \text{SFR}(z)}{\Sigma \text{SFR}(0)} = \frac{\text{SFR}(z)}{\text{SFR}(0)} (1+z)^{1.5} \quad (8)$$

The $\text{SFR}_{\nu_1} - L_{\nu_1}$ relations given in Eqs. 3 and 4 can be converted to a $\Sigma \text{SFR}_{\nu_1} - I_{\nu_2}$ expression using Eq. 6. Then, the evolution of the surface brightness with z is obtained for case (1) using Eq. 7,

$$I_{\nu_2}(z) = I(0) \frac{\text{SFR}_{\nu_1}(z)}{\text{SFR}(0)} \frac{D^2}{D_L^2} (1+z)^{1-\alpha}, \quad (9)$$

and for case (2) using Eq. 8,

$$I_{\nu_2}(z) = I(0) \frac{\text{SFR}_{\nu_1}(z)}{\text{SFR}(0)} \frac{D^2}{D_L^2} (1+z)^{2.5-\alpha}, \quad (10)$$

with $I(0)$ the surface brightness at $z = 0$ and SFR(0) the model normalization (obtained from Eq. 1 by assuming $z = 0$). For the thermal emission $\alpha = \alpha_{\text{th}}$ and for the nonthermal emission $\alpha = \alpha_{\text{nt}}$. We note that the surface brightness of the thermal emission given by Eqs. 9 and 10 does not depend on T_e provided that T_e does not vary with redshift.

The spectral index of the thermal emission is given by the Planck function that is $\alpha_{\text{th}} = 0.1$ in the optically thin condition, as expected for the ISM at ≥ 1 kpc scales. The nonthermal spectral index α_{nt} is proportional to the energy index of cosmic ray electrons. It can change depending on the cooling mechanism and interaction of cosmic ray electrons with the ISM ([Longair 1994](#)). As mentioned in Sect. 1, resolved studies show that α_{nt} is flatter in star-forming regions compared to more quiescent regions of the ISM ([Tabatabaei et al. 2007b, 2013a](#)). This is expected as cosmic rays have higher energies closer to star-forming regions and supernova remnants where they are injected. Intense star formation feedback in the form

⁴ The effective radius r_e is defined as the semi-major axis of the ellipse that contains half of the total flux of the best-fitting Sérsic model.

of relativistic shocks can also re-accelerate cosmic ray electrons, causing a flatter energy index. For the KINGFISH galaxy sample, [Tabatabaei et al. \(2017\)](#) showed that α_{nt} changes with ΣSFR as $\alpha_{\text{nt}} \sim (-0.41 \pm 0.05) \times (\log \Sigma \text{SFR})$. Hence, it is expected that α_{nt} changes with redshift due to the increase in ΣSFR :

$$\alpha_{\text{nt}}(z) = \alpha_{\text{nt}}(0) - (0.41 \pm 0.05) \log \frac{\Sigma \text{SFR}(z)}{\Sigma \text{SFR}(0)}, \quad (11)$$

with $\alpha_{\text{nt}}(0)$ the nonthermal spectral index at $z = 0$ and ΣSFR in $M_\odot\text{yr}^{-1}\text{kpc}^{-2}$.

2.3 Input data for the simulations

Eqs. 9 and 10 allow us to predict the radio surface brightness of present-day galaxies when placed at higher redshift, provided their $z \sim 0$ RC surface brightness distribution is known. Therefore, we select nearby star-forming galaxies whose RC properties are well-studied with current radio telescopes. These are M51, NGC6946, and M33 which lie within 0.4 dex of the main sequence (Table 1). Their recent SFR traced by a combination of the far-UV and infrared emission are comparable with those obtained for the main sequence galaxies (Eq. 1) at $z = 0$ taking into account their uncertainties (about 50% for hybrid SFR calibrations, [Leroy et al. 2008](#)). The galaxies selected also have decomposed maps of their thermal and nonthermal RC emission sensitive to all ISM structures down to sub-kpc scales. The data of these prototypical star-forming galaxies used to obtain $I^{\text{th}}(0)$ and $I^{\text{nt}}(0)$ are described in the following.

NGC 5194 (M 51)– is a classical grand-design spiral galaxy of Hubble type Sbc. It represents the most massive galaxy in our sample. Its iconic spiral arms are also bright in the radio. M51 emits stronger RC in the north than in the south particularly at lower frequencies ([Mulcahy et al. 2019](#)), indicating a nonthermal origin. M51 was observed with the VLA at 1.4 GHz with C-array ([Neininger & Horellou 1996](#)) and D-array ([Horellou et al. 1992](#)). These data were re-reduced and combined by [Fletcher et al. \(2011\)](#) resulting in a map sensitive to emission on all scales down to a beam size of $15''$ equivalent to a physical scale of $\simeq 0.55$ kpc. This map was decomposed into the thermal and nonthermal components using the Thermal Radio Template technique (TRT, [Tabatabaei et al. 2007b, 2013a](#), see also Appendix). This method uses no prior assumptions about the RC spectrum as mentioned in Sect. 1.

NGC 6946– is a late-type Scd spiral galaxy. It is less massive than M51 but has a higher specific SFR. The distri-

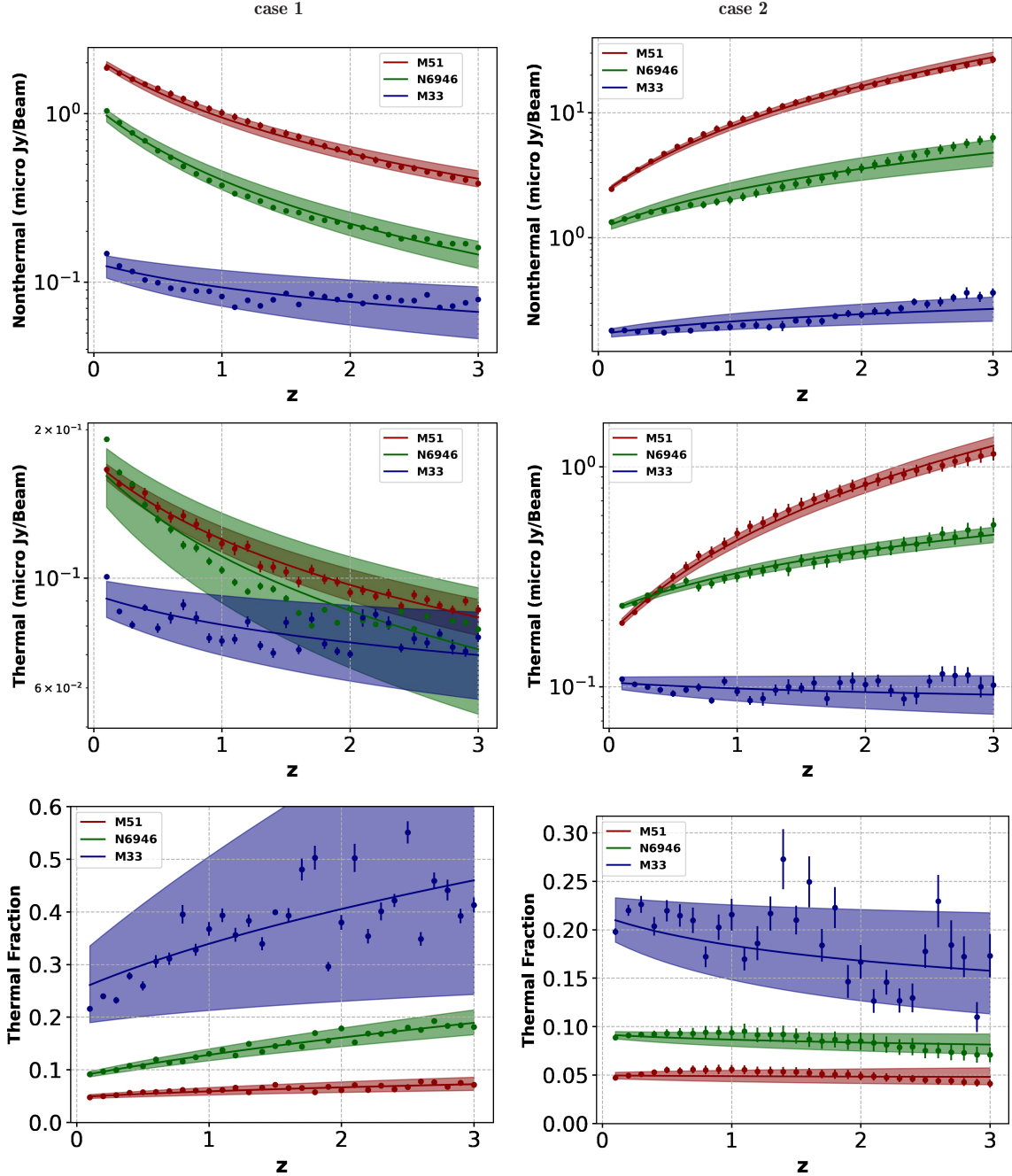


Figure 1. Redshift evolution of the nonthermal ($I_{\nu_2}^{\text{nt}}$) (top) and thermal ($I_{\nu_2}^{\text{th}}$) (middle) mean surface brightness and the corresponding thermal fraction, ($f_{\nu_2}^{\text{th}}$), (bottom) for case 1 (left) and case 2 (right) at the observed frequency of $\nu_2 = 1.4$ GHz (equivalent to a rest-frame frequency of 1.6–5.6 GHz at $0.15 \leq z \leq 3$). The mean values of the maps simulated with the UDT-noise sky level (points) are shown with their standard errors σ/\sqrt{n} , where σ is the standard deviation and n the number of map pixels. Curves are fitted functions of the form $a(1+z)^b$ with a and b listed in Table 4. Shaded regions show the 3σ uncertainties of the fits.

tribution of star formation is asymmetric with one prominent spiral arm in the north-east. Its spiral arms are generally not as prominent as those of M51 indicating weaker density waves (Cedr es et al. 2013). NGC 6946 has been extensively studied in the radio (see Beck 2007, and references therein). This study uses the combined VLA C- and D- array observations at 1.4 GHz (Beck 1991) at an angular resolution of $15''$ (equivalent to a physical scale of $\simeq 0.5$ kpc at its

6.8 Mpc distance). The thermal/nonthermal decomposition of this map was presented by Tabatabaei et al. (2013a) based on the TRT method at $\simeq 0.6$ kpc linear resolution.

NGC 598 (M 33)– is a low-surface brightness Scd spiral galaxy with a flocculent structure. Residing between the dwarfs and normal spirals (e.g., Shao et al. 2018; Mueller & Jerjen 2020), galaxies like M33 are important to assess capabilities of the SKA surveys in detecting the ISM in

low-mass, low-surface brightness galaxies at high-redshifts⁵. M33 was observed with the VLA at 1.4 GHz in D-array (Tabatabaei et al. 2007a). As the VLA primary beam of 30' (at 1.4 GHz) is smaller than the apparent galaxy size ($\simeq 70'$), a mosaic of 12 pointings was used to cover the entire galaxy. The final VLA map has an angular resolution of 51'' equivalent to a physical scale of $\simeq 0.2$ kpc at its 840 kpc distance. To recover the extended emission or correct for missing short spacing, the VLA map was combined with the Effelsberg 100-m observations at the same frequency (Tabatabaei et al. 2007a). We presented the TRT thermal/nonthermal separation in Tabatabaei et al. (2013b).

The thermal and nonthermal emission obtained for these galaxies⁶ serve as the input data $I^{\text{th}}(0)$ and $I^{\text{nt}}(0)$ in Eqs. (9) and (10) to obtain the surface brightness maps at other redshifts taking into account the geometrical effects.

2.4 SKA reference surveys

A main goal of this study is to predict the structure of the RC emitting ISM in distant normal star-forming galaxies as observed with the proposed SKA reference surveys. In phase 1, SKA will offer observations for three of the five bands covering the frequency range 0.35-13.8 GHz (SKA1-MID), specifically band 1 (350-1000 MHz), band 2 (950-1760 MHz) and band 5 (4.6-13.8 GHz). However, SKA1-MID continuum reference surveys are proposed only for band 2 and band 5 to achieve high-angular resolutions resolving high-redshift galaxies at 0.05''–0.5'' (Prandoni & Seymour 2015, hereafter PS15)⁷. We investigate the compatibility with the band 2 survey centered at $\simeq 1.4$ GHz, because our input data are mostly available at this frequency. The band 2 survey is a *Three-tiered survey* aiming to observe a set of fields of views (FoVs) on the sky with different depths. The FoVs are about 1000 deg², 10 deg², and 1 deg² reaching a sky level (rms sensitivity) of 1 μ Jy, 0.2 μ Jy, and 0.05 μ Jy in the wide tier (WT), deep tier (DT), and ultra-deep tier (UDT), respectively. PS15 calculated the time needed to achieve these depths using the full-bandwidth available. They assumed an angular resolution of 0.5''. However, we note that it will be possible to sample angular scales down to $\sim 0.35''$ in band 2 given the 150 km maximum baseline of SKA1-MID (see Fig. 10 in the System Baseline description published by the SKA office⁸). At this maximum resolution, the sensitivity is, however, reduced compared to lower resolutions. We also note that the final image resolution depends both on frequency and also the weighting method used by the imaging pipeline. In this paper, we adopt the smallest angular scale at which the MID array provides maximal sensitivity in band 2, that is $\theta_{\text{SKA}} = 0.6''$. At this resolution, the above sky levels will be achieved earlier than the observing time proposed by PS15 (e.g., 3300 hours per pointing for UDT).

⁵ Lower mass dwarf galaxies are not considered in this study as they are hardly detectable at high- z with the proposed SKA1-MID surveys (see Sect. 4.3).

⁶ The maps are shown in the first rows of Figs. 2, 3 and 4.

⁷ Band 1 provides lower angular resolutions of about 0.7''

⁸ http://skacontinuum.pbworks.com/w/file/attach/119268525/SKA-TEL-SKO-0000308_SKA1_System_Baseline_v2_DescriptionRev01-part-1-signed.pdf

2.4.1 Thermal/nonthermal separation methods with SKA1-MID

As mentioned in Sect. 1, mapping the thermal and non-thermal components of the RC emission requires a proper frequency sampling, particularly at the low and high frequency ends, with consistent sensitivities. This becomes more vital for resolved studies addressing the evolution of the thermal and nonthermal surface brightness in distant galaxies. Particularly, band 1 provides an important constrain on the mid-radio SEDs when studying the epoch of maximum star formation rate at $z \approx 2$ (see Sect. 4.2). Therefore, the currently proposed Band 2 & 5 surveys will not be sufficient for a radio-based separation in distant galaxies. Avoiding any assumption about the radio SED, the TRT technique (Tabatabaei et al. 2007b, 2013a) (see Appendix) can be ideally used at a single radio frequency. This will be feasible using deep narrow-band or spectroscopy imaging surveys of recombination lines tracing the free-free emission at resolutions comparable with those of the SKA.

2.5 Simulating maps at high redshifts

The maps of the thermal and nonthermal surface brightness $I_{\nu_2}^{\text{th}}(z)$ and $I_{\nu_2}^{\text{nt}}(z)$ of M51-, NGC6946-, and M33-like galaxies are simulated over the redshifts $0 < z \leq 3$ where the main sequence typically spans the mass range of galaxies selected ($\simeq 10^{9.5} - 10^{10.6} M_{\odot}$, Schreiber et al. 2015). Depending on redshift, the change in apparent size of a galaxy observed in a fixed FoV of the telescope, i.e., the redshift dependence of angular scales, geometrical effects, and instrumental resolution must be taken into account. The simulated maps should also contain noise to mimic real observations. How we account for these effects is explained in the following.

2.5.1 Geometrical effects

The radio continuum maps simulated at high redshifts should resemble those that will be observed by SKA with an angular resolution of θ_{SKA} . Thus, the angular resolutions and pixel sizes of the $I(0)$ maps should be converted to those of the SKA observations. Because the radio measurements are per unit beam area, this is done by first convolving the maps to the angle subtended to redshift z by the linear resolution element x of the nearby galaxy at distance D and the resulting map is then resampled. Considering that $\tan(\theta) \simeq \theta$ for a small angle, the linear scale element x for case (1) is given by

$$x = \theta(z) \frac{D_L}{(1+z)^2} = \theta_0 \frac{D}{(1+z)^2}, \quad (12)$$

with $\theta(z)$ and θ_0 the angles subtended by x at redshifts z and $z_0 \simeq 0$ in units of radian. Hence, the angle representing the physical resolution of the $I(0)$ maps at redshift z is given by

$$\theta(z) = \theta_0(1+z)^2 \frac{D}{D_L}. \quad (13)$$

For case (2), x changes with redshift as a result of the galaxy size evolution, thus $x = x_0(1+z)^{-0.75}$ with x_0 the linear resolution element at $z = 0$. This leads to

$$\theta(z) = \theta_0(1+z)^{1.25} \frac{D}{D_L}. \quad (14)$$

Galaxy	z	$\langle I_{\nu_2}^{\text{nt}} \rangle$	$\langle I_{\nu_2}^{\text{th}} \rangle$	$\langle I_{\nu_2}^{\text{tot}} \rangle$	$\langle f_{\nu_2}^{\text{th}} \rangle$	$\langle S/N_{\text{UDT}} \rangle$	$\langle S/N_{\text{DT}} \rangle$	$\langle S/N_{\text{WT}} \rangle$
M 51	0.15	1790±39	155±3	1945±42	0.048±0.001	43	11	2
	0.3	1600±51	154±3	1754±54	0.051±0.002	39	10	2
	0.5	1409±55	139±3	1548±58	0.057±0.002	34	8	2
	1	1011±47	117±3	1058±50	0.059±0.003	24	6	1
	2	589±27	93±2	682±29	0.061±0.002	15	4	< 1
NGC 6946	0.15	957±18	177±2	1134±20	0.095±0.002	23	6	1
	0.3	769±21	155±3	924±24	0.099±0.002	18	4	< 1
	0.5	603±21	131±2	734±23	0.106±0.003	14	4	< 1
	1	374±14	104±2	478±16	0.130±0.004	9	2	< 1
	2	214±7	87±1	301±8	0.178±0.004	5	1	< 1
M 33	0.15	133±2	89±1	222±3	0.224±0.004	4	< 1	< 1
	0.3	115±2	80±1	195±3	0.231±0.006	3	< 1	< 1
	0.5	99±3	79±2	178±5	0.259±0.009	2	< 1	< 1
	1	82±2	74±2	156±4	0.367±0.013	2	< 1	< 1
	2	83±2	70±1	153±3	0.380±0.014	1	< 1	< 1

Table 2. Mean surface brightness of the nonthermal ($\langle I_{\nu_2}^{\text{nt}} \rangle$), thermal ($\langle I_{\nu_2}^{\text{th}} \rangle$), and total ($\langle I_{\nu_2}^{\text{tot}} \rangle$) radio continuum maps simulated with the UDT-noise sky level in unites of nJy (10^{-9} Jy)/beam at 5 selected redshifts for case (1) (no radio size evolution) at the observed frequency of 1.4 GHz. Also listed are the mean thermal fraction ($\langle f_{\nu_2}^{\text{th}} \rangle$) and the signal-to-noise ratio (see Sect. 4.3) for the SKAI-MID band2 UDT ($\langle S/N_{\text{UDT}} \rangle$), DT ($\langle S/N_{\text{DT}} \rangle$), and WT ($\langle S/N_{\text{WT}} \rangle$).

Galaxy	z	$\langle I_{\nu_2}^{\text{nt}} \rangle$	$\langle I_{\nu_2}^{\text{th}} \rangle$	$\langle I_{\nu_2}^{\text{tot}} \rangle$	$\langle f_{\nu_2}^{\text{th}} \rangle$	$\langle S/N_{\text{UDT}} \rangle$	$\langle S/N_{\text{DT}} \rangle$	$\langle S/N_{\text{WT}} \rangle$
M 51	0.15	2707±64	206±4	2913±68	0.048± 0.001	64	16	3
	0.3	3497±131	248±7	3745±138	0.050±0.002	80	20	4
	0.5	4704±231	315±14	5019±245	0.055±0.003	103	26	5
	1	8194±479	499±28	8693±507	0.056±0.005	174	43	9
		16202±1063	835±54	17037±1117	0.049±0.005	341	85	17
NGC 6946	0.15	1372±29	240±4	1612±33	0.089±0.002	34	8	1
	0.3	1485±54	261±6	1746±60	0.092±0.003	37	9	2
	0.5	1650±86	284±10	1934±96	0.093±0.004	40	10	2
	1	2006±152	316±17	2322±169	0.094±0.07	50	12	3
	2	3601±320	409±31	4010±351	0.085±0.009	83	21	4
M 33	0.15	179±3	106±1	285±4	0.195± 0.004	5	1	< 1
	0.3	178±6	100±3	278±9	0.226±0.009	5	1	< 1
	0.5	174±8	93±3	267±11	0.220±0.011	5	1	< 1
	1	193±13	95±4	288±17	0.216±0.005	6	1	< 1
	2	242±16	102±5	344±21	0.167±0.005	7	2	< 1

Table 3. Same as Table 2 for case (2) (radio size evolution with z).

Given that $\theta(z)$ represents the original angular resolution at redshift z , the maps are then convolved using a Gaussian kernel with the width of $\sqrt{\theta_{\text{SKA}}^2 - \theta(z)^2}$ for each case (1) and (2) resulting in maps at the SKA resolution⁹. These maps are then re-sampled to have 4 pixels per beam at each redshift. As a result, the number of pixels reduces with redshift and the maps become more unresolved. To keep the observation

FoV unchanged, we add more number of pixels as sky to the surrounding of the maps. Therefore, the final maps simulated have the same number of pixels at different redshifts.

2.5.2 Adding noise

The radio images simulated inherit the background noise from the VLA¹⁰ observations. However, as the noise val-

⁹ This means that we can start the simulations from the redshifts at which $\theta(z) < \theta_{\text{SKA}}$.

¹⁰ VLA & Effelsberg for M33

Galaxy	Component	$a^{(1)}$	$b^{(1)}$	$a^{(2)}$	$b^{(2)}$
M 51	$\langle I_{\nu_2}^{\text{nt}} \rangle$	2.18 ± 0.09	-1.21 ± 0.05	2.12 ± 0.07	1.86 ± 0.04
	$\langle I_{\nu_2}^{\text{th}} \rangle$	0.17 ± 0.006	-0.52 ± 0.04	0.17 ± 0.005	1.43 ± 0.05
	$\langle f_{\nu_2}^{\text{th}} \rangle$	0.05 ± 0.003	0.30 ± 0.08	0.05 ± 0.003	-0.02 ± 0.09
NGC 6946	$\langle I_{\nu_2}^{\text{nt}} \rangle$	1.12 ± 0.08	-1.47 ± 0.08	1.16 ± 0.08	1.02 ± 0.12
	$\langle I_{\nu_2}^{\text{th}} \rangle$	0.17 ± 0.02	-0.63 ± 0.12	0.22 ± 0.005	0.58 ± 0.04
	$\langle f_{\nu_2}^{\text{th}} \rangle$	0.09 ± 0.004	0.56 ± 0.05	0.09 ± 0.003	-0.09 ± 0.07
M 33	$\langle I_{\nu_2}^{\text{nt}} \rangle$	0.13 ± 0.02	-0.48 ± 0.16	0.17 ± 0.01	0.34 ± 0.11
	$\langle I_{\nu_2}^{\text{th}} \rangle$	0.09 ± 0.007	-0.20 ± 0.09	0.10 ± 0.006	-0.09 ± 0.10
	$\langle f_{\nu_2}^{\text{th}} \rangle$	0.25 ± 0.06	0.44 ± 0.25	0.21 ± 0.02	-0.22 ± 0.17

Table 4. Fit parameters a and b of the functional form $a(1+z)^b$ shown in Fig. 1. The parameters are obtained using a least-square regression. Indices (1) and (2) represent case 1 and case 2, respectively.

ues are much smaller than the signal from the galaxy in the original maps, the simulated maps are practically noiseless. It is then important to add background noise due to the SKA observations. According to the anticipated SKA1 science performance (Braun et al. 2019), the image noise depends on the sensitivity of the antennas, correlator efficiency, frequency bandwidth, and integration time. Moreover, as a source of correlated noise, the dirty synthesized beam pattern is determined by the array configuration, the (u,v) coverage of observation and the data weighting scheme that is employed. The (u,v) coverage and data weighting scheme are given by the observing strategy and are thus up to the user. The sensitivity of the images is set in accordance with the SKA1-MID reference surveys outlined in Sect. 2.4. We inject the 1σ rms sky levels of the *Three-tiered Band 2 Survey* into our simulated total RC (= thermal + nonthermal) maps after generating Gaussian noise of those levels¹¹. A more realistic noise treatment can include other instrumental correlated noise that is unknown at this stage for the SKA. Sky levels injected are the same for the thermal and nonthermal radio maps that is expected if the radio SED method is used to separate these RC components. We note that using the TRT separation method (Sect. 2.4.1) instead, the sky level in the thermal radio map can differ depending on the map of the free-free emission template (e.g., H α emission).

3 RESULTS

Following Sect. 2, the thermal and nonthermal surface brightness maps are generated at all redshifts in the range $0 < z \leq 3$ with $\Delta z = 0.1$ at the observed frequency $\nu_2 = 1.4$ GHz for cases (1) and (2). Our findings are presented by first looking at variations in the galaxy mean values with z and then describing structures observed at selected redshifts. These results are mainly based on the maps with the UDT-noise sky level but Tables 2 and 3 also report signal-to-noise ratios for the DT and WT sky levels.

3.1 Redshift evolution

To investigate the redshift evolution of the mean surface brightnesses $\langle I_{\nu_2}^{\text{th}} \rangle$ and $\langle I_{\nu_2}^{\text{nt}} \rangle$, the thermal and nonthermal maps are averaged at each z . The resulting redshift evolution of $\langle I_{\nu_2}^{\text{th}} \rangle$ and $\langle I_{\nu_2}^{\text{nt}} \rangle$ are then plotted (Fig. 1) and the corresponding values at selected redshifts $z = 0.15, 0.3, 0.5, 1, 2$ are listed in Table 2 for case (1) and Table 3 for case (2). The errors in the mean values reported are the statistical errors, i.e., the square root of the standard deviation around the mean divided by the number of pixels in each map. To illustrate better the global evolutionary trends, we fitted functions of the form $a(1+z)^b$ to the distribution of the surface brightness vs. z (curves in Fig. 1) using a least-square regression with parameters listed in Table 4. We find that, in case (1), the nonthermal surface brightness ($I_{\nu_2}^{\text{nt}}$) drops globally with z for all 3 kinds of galaxies, although there are some fluctuations particularly at $z > 1$ in low-mass M33-like galaxies. The thermal emission surface brightness ($\langle I_{\nu_2}^{\text{th}} \rangle$) exhibits more fluctuations than $\langle I_{\nu_2}^{\text{nt}} \rangle$ but it also drops globally with z . This global change is faster in more massive galaxies. In case (2), the trends should be reversed because the sizes shrink with z . This is observed for $\langle I_{\nu_2}^{\text{nt}} \rangle$ in all galaxies but only in M51- and NGC6946-like galaxies for $\langle I_{\nu_2}^{\text{th}} \rangle$. No certain global trend is found for $\langle I_{\nu_2}^{\text{th}} \rangle$ in low-mass M33-like galaxies ($b^{(2)} = -0.09 \pm 0.10$). We note that, in these galaxies, the thermal emission signal predicted is generally not robust because it is close to the sky level fluctuations injected (e.g., $0.05 \mu\text{Jy}/\text{beam}$ for UDT, see also $\langle I_{\nu_2}^{\text{th}} \rangle$ in Tables 2 and 3).

The mean thermal fraction defined as $\langle f_{\nu_2}^{\text{th}} \rangle = \langle I_{\nu_2}^{\text{th}} \rangle / \langle I_{\nu_2}^{\text{tot}} \rangle$, with $\langle I_{\nu_2}^{\text{tot}} \rangle = \langle I_{\nu_2}^{\text{th}} \rangle + \langle I_{\nu_2}^{\text{nt}} \rangle$ is also calculated and plotted against z (Fig 1). In case (1), $\langle f_{\nu_2}^{\text{th}} \rangle$ follows a global increase. From $z = 0.15$ to $z = 2$, $\langle f_{\nu_2}^{\text{th}} \rangle$ increases by $\simeq 30\%$ in galaxies like M 51. The increase is faster in NGC 6946- and M33-like galaxies by about a factor of two as shown by their fitted slope b being larger than that of M 51. Again, we caution that the evolution of $\langle f_{\nu_2}^{\text{th}} \rangle$ in M 33-like galaxies is not as certain due to low signal-to-noise ratios and large fluctuations particularly at $z \gtrsim 0.7$.

In case (2), the mean thermal fraction increases slightly from $z = 0.15$ to $z \simeq 1$, then decreases by about the same rate from $z = 1$ to $z = 3$ in M 51- and NGC 6946-like galaxies. This occurs because the increase of the non-thermal emission is faster than that of the thermal emission at $z > 1$. Hence, the fitted single-slope function shows almost no evo-

¹¹ using the task `numpy.random.normal` in Python version 3.0.

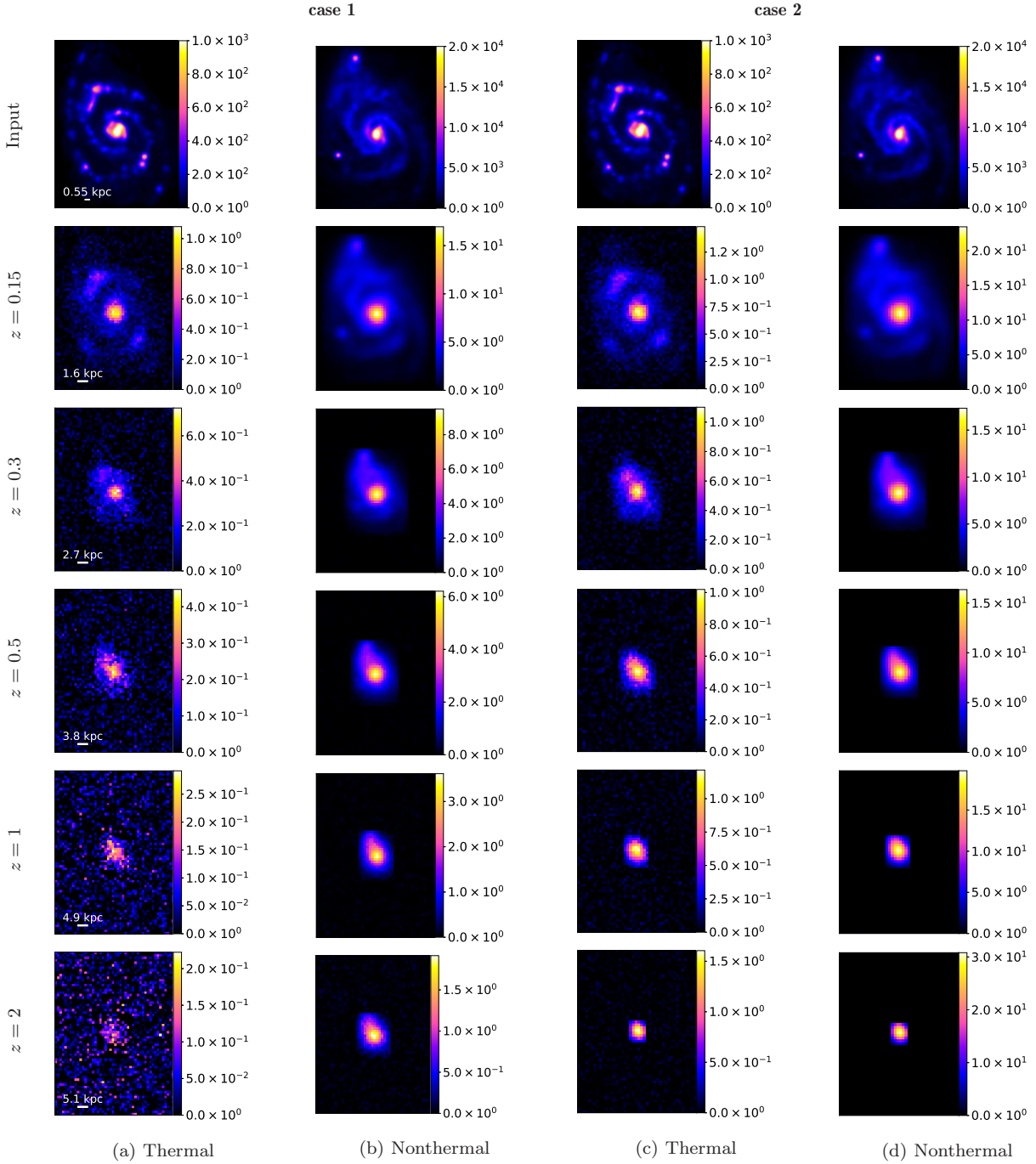


Figure 2. Simulated surface brightness maps for a M51-like galaxy with the UDT-noise sky level at the observed frequency of 1.4 GHz showing the case(1)-thermal emission (*first column*), case(1)-nonthermal emission (*second column*), case(2)-thermal emission (*third column*), and case(2)-nonthermal emission (*fourth column*) at $z = 0.15, 0.3, 0.5, 1,$ and 2 from the second to last row, respectively. First row shows the thermal and non-thermal maps of M51 separated (following [Tabatabaei et al. 2007b](#)). Bars show the surface brightness in units of $\mu\text{Jy}/\text{beam}$.

lution from $z = 0$ to $z = 3$. In M33-like galaxies, the global decrease of $\langle f_{\nu_2}^{\text{th}} \rangle$ occurs because of the increase in $\langle I_{\nu_2}^{\text{nt}} \rangle$. However, this evolution inherits the large uncertainty in $\langle I_{\nu_2}^{\text{th}} \rangle$ at high redshifts.

Over the redshift range of $z = 0.15 - 3$, a lower thermal fraction ($f_{\nu_2}^{\text{th}}$) is found in more massive galaxies. These results are further discussed and compared with the literature in Sect. 4.4.

3.2 Maps at selected redshifts

Figures 2 to 4 show the maps of the thermal and nonthermal surface brightness, $I_{\nu_2}^{\text{th}}(z)$ and $I_{\nu_2}^{\text{nt}}(z)$, for galaxies like M51, NGC6946, and M33 at selected redshifts of $z = 0.15, 0.3, 0.5,$

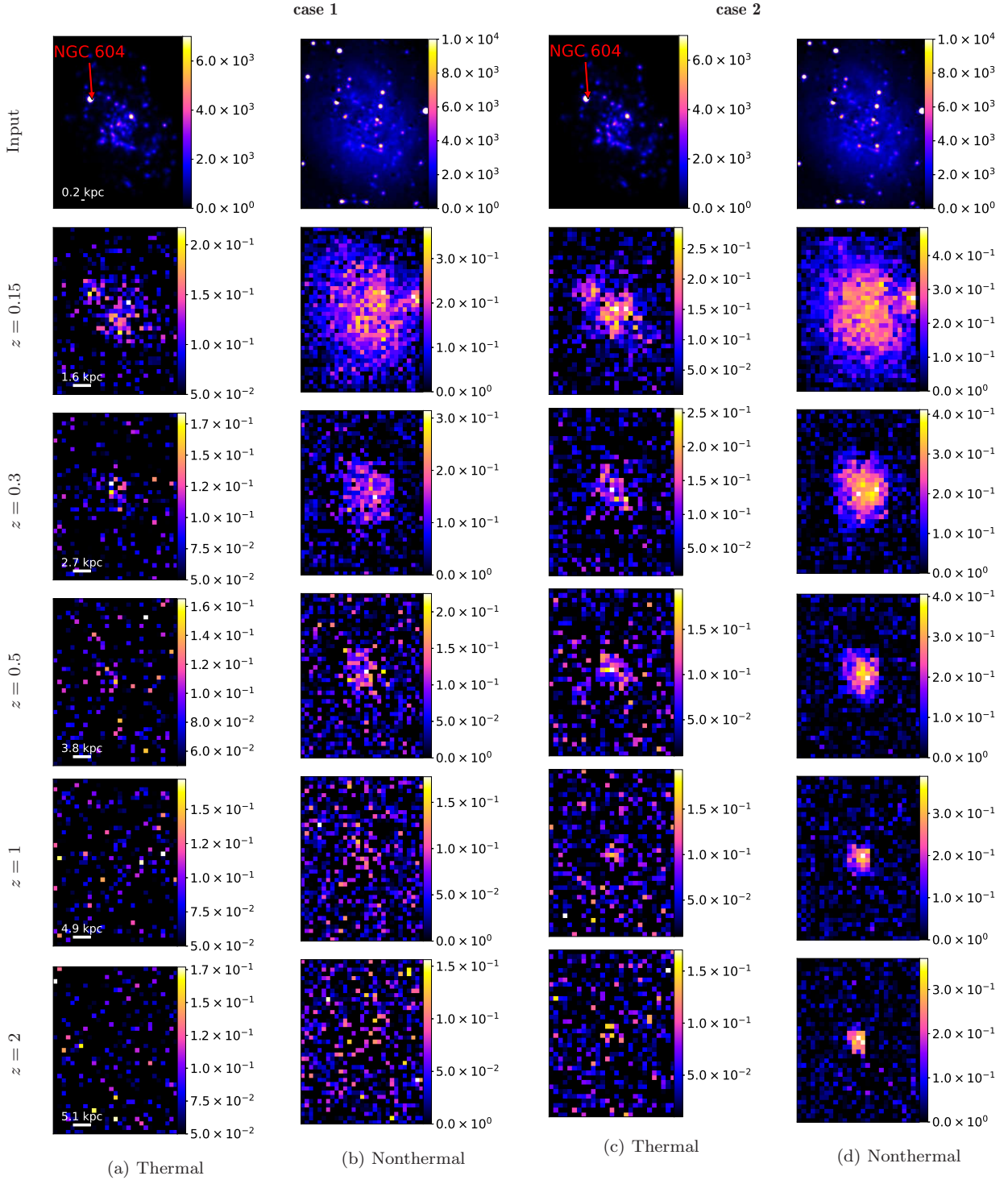


Figure 4. Same as Fig. 2 for M33-like galaxy. First row shows the thermal and non-thermal maps of M33 (from Tabatabaei et al. 2013b). Bars show the surface brightness in units of $\mu\text{Jy}/\text{beam}$.

redshift. The inner disk is always the most luminous part of the galaxy in both cases. The thermal emission from the disk becomes closer to the sky level with increasing z in case (1), while it is well above it ($\gtrsim 10\sigma$) in case (2).

- NGC 6946-like galaxies: As shown in Fig. 3, the thermal maps are dominated by bright clumps corresponding to giant HII complexes (including the one in its nucleus) which

remains visible at redshifts $z = 0.15$ and $z = 0.3$. In case (1), the spiral arms can also be traced up to $z = 0.3$. The nonthermal map, however, exhibits a clumpy structure at $z = 0.15$ which becomes smoother at $z = 0.3, 0.5$. Only unresolved disks with a smooth decrease of brightness toward the outer disk are observable at $z = 1$ and higher. In case (1), the nonthermal emission from the outer disk gets below the detection threshold at $z = 2$ and

the thermal emission can hardly be detected even at the center ($\lesssim 4\sigma$). At this redshift, the information from the entire disk is preserved in case (2), although the disk has a smaller physical dimension than in the other case. The thermal fraction in bright star-forming regions is above 15% (reaching to 30%) in case (1) but it falls below 12% at $z = 2$ in case (2). Similar to M51-like galaxies, $f_{\nu_2}^{\text{th}}$ is always below the mean galaxy value ($\langle f_{\nu_2}^{\text{th}} \rangle$) in the center due to a strong nonthermal component (Tabatabaei et al. 2013a).

- M33-like galaxies: The surface brightness of the RC emission is much weaker than that in other galaxy types, hence, the maps simulated are noisier generally (Fig. 4). The structures are severely affected by noise fluctuations and galaxies cannot be distinguished at $z = 1, 2$ in case (1). By $z = 0.15$, giant HII regions such as NGC 604 can be traced in the thermal emission, while the nonthermal map exhibits an extended bright diffuse disk. This disk remains visible out to $z = 2$ in case (2). Similar to their more massive counterparts, these galaxies show a higher thermal fraction in star-forming regions than in other regions of the ISM (e.g., at $z = 0.15$, $f_{\nu_2}^{\text{th}}$ exceeds from 30% in star-forming regions).

4 DISCUSSION

In this section, we discuss the redshift evolution of the non-thermal emission spectral index and the mid-radio SED. We then address the detectability of kpc-scale emission from high-redshift objects similar to present-day galaxies with the planned SKAI-MID surveys. Finally, we compare our findings with observational results in the literature.

4.1 Evolution of the nonthermal spectral index

As shown by Tabatabaei et al. (2017), the nonthermal spectrum at mid-radio frequencies ($1 < \nu < 10$ GHz) flattens with increasing star formation density in normal star-forming galaxies. This was explained by cosmic ray electrons being more energetic in galaxies with higher star formation activity. In other words, these particles are not much affected by cooling because of the topology of the magnetic field: massive star formation produces more turbulent and tangled magnetic fields. High-energy cosmic ray electrons injected in star-forming regions scatter off the very many pitch angles of the tangled field causing winds and outflows due to pressure gradients. Thus, their energy spectrum remains globally flatter as winds can diffuse high energy CREs on timescale shorter than those of synchrotron cooling. It is interesting to note that a flattening was also reported in highly star-forming galaxies (HSFGs) at high redshifts ($z \in [0.3, 4]$, $\text{SFR} \geq 100 M_{\odot} \text{yr}^{-1}$) in the VLA-COSMOS 3 GHz Large Project by Tisanić et al. (2019). These authors found a mean spectral index of $\simeq 0.42$ at $\langle z \rangle = 1.7 \pm 0.6$ that is much flatter than that found for nearby normal star forming galaxies with $\text{SFR} \leq 10 M_{\odot} \text{yr}^{-1}$ ($\alpha_{\text{nt}} \simeq 0.9$, Tabatabaei et al. 2017). Did the present-day normal star forming galaxies have a flatter α_{nt} in the past when their SFR was higher?

Following Eq. 11, we obtain the evolution of the non-thermal spectral index α_{nt} for galaxies like M51, NGC6946, and M33 for which the local values of $\alpha_{\text{nt}}(0)$ are listed in

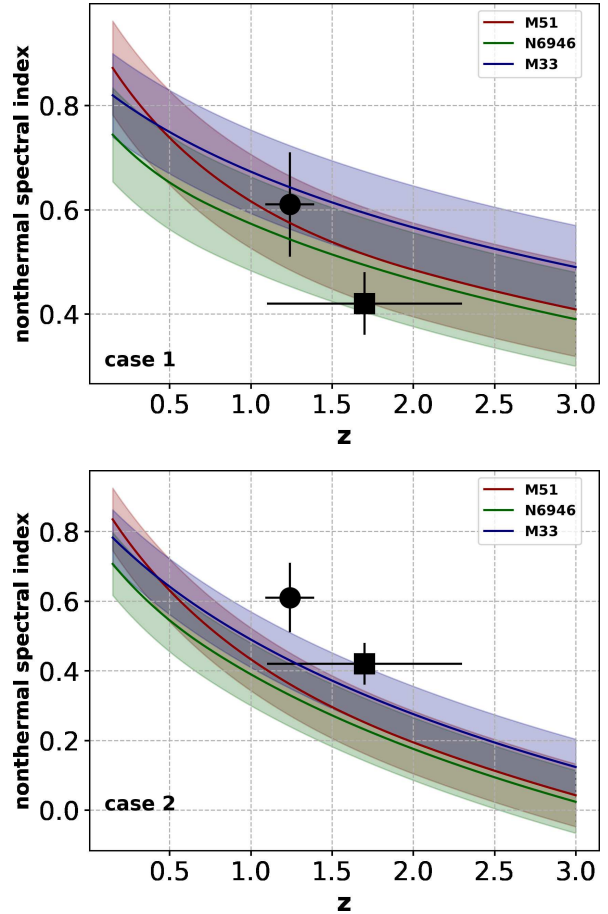


Figure 5. Evolution of the spectral index α_{nt} with redshift for case 1 (top) and case 2 (bottom). Shaded bands show errors in the spectral indices given in Table 1. Points indicate the measurements based on observations (circle: Murphy et al. 2017) and (square: Tisanić et al. 2019) showing a better agreement with case 1 (no radio size evolution).

Table 1. As shown in Fig. 5, α_{nt} drops with redshift in both evolutionary cases (1) and (2), but with a different redshift dependence. It drops from 0.8-0.9 to 0.5-0.6 from $z = 0$ to $z = 2$ in case (1), and even faster in case (2). The errors shown in Fig. 5 represent measurement errors in $\alpha_{\text{nt}}(0)$ (see Table 1). However, we note that the main source of uncertainty in Eq. 11 is due to $\text{SFR}(z)$ having a scatter of 0.3 dex. As α_{nt} reflects the energy index of cosmic ray electrons, the evolutionary trends obtained imply that these particles were more energetic at redshifts when galaxy star formation rates were higher and supernova explosions more frequent.

Besides the results based on the VLA-COSMOS observations of HSFGs (Tisanić et al. 2019), the VLA observations of the μJy radio sources observed in the GOODS-N field also show a flatter spectrum at high z ($\simeq 0.61$ at $\langle z \rangle = 1.24 \pm 0.15$, Murphy et al. 2017). This sample has a mean SFR of $\sim 25 M_{\odot} \text{yr}^{-1}$ at $z \sim 1$ (Murphy et al. 2017), similar to that of a M51-like galaxy at the same redshift (see Table 1). Hence, a better agreement of our predictions is expected with the VLA GOODS-N than with the VLA-COSMOS survey. The mean values of the spectral indices

measured by both surveys are overlaid in our simulations in Fig 5. The GOODS-N measurement (Murphy et al. 2017) agrees with the case (1) simulation, particularly for M51-like galaxies as expected, while it is steeper than that of the case (2) predictions. Due to their higher SFR, the VLA-COSMOS measurements (Tisanić et al. 2019) should be flatter than the prediction of the M51-like galaxies at the same z . This is nicely seen in case (1). Therefore, these observations are in favor of no (or a shallow) evolution of the radio size of galaxies.

We note that observational studies of the evolution of the spectral index can be complicated by *a*) contamination by thermal emission, *b*) large observational uncertainties and inconsistent sensitivities at different frequencies, (noting that the uncertainty in measuring the spectral index is often $\simeq 25\%$), and *c*) the presence of obscured steep spectrum AGNs that are likely to be more abundant at higher redshifts (e.g. Magnelli et al. 2015; Ivison et al. 2010; Bourne et al. 2011; An et al. 2021). We note that AGNs can complicate any correlation between the spectral index and z in unresolved studies. The observed radio spectrum of AGNs can be flat at low redshifts $\alpha < 0.5$ (eg., Murphy et al. 2013) but steep at high redshifts $\alpha > 1$ (e.g., Huynh et al. 2007). Radio galaxies also do not obey the $\alpha_{\text{nt}} - z$ trend used here because their radio spectrum steepens at high z (e.g., Ishwara-Chandra et al. 2010; Roettgering et al. 1994; Singh et al. 2014). Overcoming all these limitations requires sensitive multi-frequency radio observations and hints on the important role of next generation radio telescopes such as the SKA.

4.2 Evolution of the radio spectral energy distribution

The evolution of the spectral index means that the rest-frame radio SED of galaxies changes with redshifts. This is investigated for the integrated mid-radio SED of a M51-like galaxy with known integrated flux densities of the thermal S_{ν}^{th} and the nonthermal S_{ν}^{nt} emission at various frequencies 1.4, 2.7, 4.8, 8.4, 10.7 GHz at $z = 0$ (Table 5). The corresponding integrated flux densities at other redshifts observed at frequencies ν_2 can be obtained following Eq. 5. In rest-frame, we have $S_{\nu_1}(z) = S_{\nu_2}(z) (\nu_1/\nu_2)^{-\alpha} = S_{\nu_2}(z) (1+z)^{-\alpha}$, with ν_1 the rest-frame frequency. Thus, the total integrated RC flux density ($S_{\nu_1} = S_{\nu_1}^{\text{th}} + S_{\nu_1}^{\text{nt}}$) evolves with redshift as

$$S_{\nu_1}(z) = \left[S_{\nu_1}^{\text{th}}(0) (1+z)^{-2\alpha_{\text{th}}} + S_{\nu_1}^{\text{nt}}(0) (1+z)^{-2\alpha_{\text{nt}}} \right] \times \frac{\text{SFR}(z)}{\text{SFR}(0)} (1+z) \frac{D^2}{D_L^2}, \quad (15)$$

with $S_{\nu_1}^{\text{th}}(0)$ and $S_{\nu_1}^{\text{nt}}(0)$ the integrated thermal and nonthermal flux densities at $z = 0$ (note that $\nu_1 = \nu_2$ at $z = 0$). The nonthermal spectral index α_{nt} is given by Eq. 11 and $\alpha_{\text{th}} = 0.1$ (see Sect. 2.2). Using Eq. 15 at different frequencies, the intrinsic flux densities can be obtained and the mid-radio (1-10 GHz) SEDs can be constructed at different redshifts. We model the SEDs following Tabatabaei et al. (2017),

$$I_{\nu} = A_1 \nu_0^{-0.1} \left(\frac{\nu}{\nu_0} \right)^{-0.1} + A_2 \nu_0^{-\alpha_{\text{nt}}} \left(\frac{\nu}{\nu_0} \right)^{-\alpha_{\text{nt}}} \quad (16)$$

with A_1 and A_2 the scaling factors, ν_0 the reference frequency, and α_{nt} given by Eq. 11. We selected $\nu_0 = 1.4$ GHz at all

Frequency (GHz)	$S_{\nu}^{\text{th}}(0)$ (mJy)	$S_{\nu}^{\text{nt}}(0)$ (mJy)
1.4	70 ± 5	1330 ± 109
2.7	66 ± 4	714 ± 66
4.8	62 ± 3	358 ± 25
8.4	58 ± 3	248 ± 20
10.7	57 ± 4	178 ± 18

Table 5. The integrated flux density of the thermal ($S_{\nu}^{\text{th}}(0)$) and nonthermal ($S_{\nu}^{\text{nt}}(0)$) emission from M51 (from Tabatabaei et al. 2017).

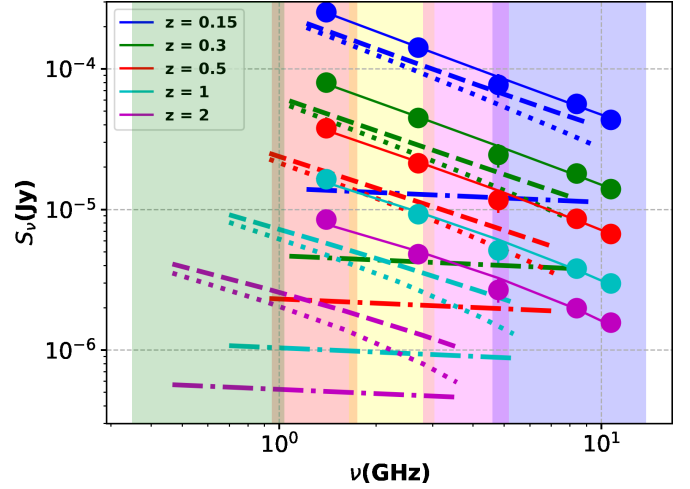


Figure 6. The fitted rest-frame SEDs (solid lines) of a M51-like galaxy at 5 different redshifts. Points show the rest-frame integrated flux densities at 1.4, 2.7, 4.8, 8.4, 10.7 GHz obtained following Eq. 15 at different redshifts. The SEDs were fitted following Eqs. 16 and 11 taking into account the errors in the fluxes (smaller than the symbols). Also shown are the corresponding SEDs in the observer-frame (dashed lines) and their thermal (dashed-dotted lines) and nonthermal (dotted lines) components. Vertical colored shades show the SKA frequency bands 1 (green), 2 (red), 3 (yellow), 4 (pink), and 5 (blue).

redshifts. A non-linear least square fit is used to obtain A_1 and A_2 at each z (by adopting the task curve_fit in Python). Figure 6 shows the resulting SEDs at selected redshifts of $z = 0.15, 0.3, 0.5, 1, \text{ and } 2$. As expected, the SEDs become flatter towards higher z . As the flattening is due to the synchrotron emission it mainly occurs at lower frequencies leading to a more pronounced curvature at higher z .

We note that these mid-radio SEDs are shifted to lower frequencies in the observer-frame. For instance, to study the intrinsic mid-radio SED of galaxies at $z < 0.5$, observations with the SKA Bands 2, 3, 4, and 5 are required. Moving to higher redshifts, SKA Band 1 becomes important as well. At $z = 2$, the intrinsic mid-radio SED can be studied through Bands 1 to 4. The corresponding observed SEDs along with the SKA frequency windows are shown in Fig. 6. The offset between the observed and the rest-frame SEDs increases with redshift.

4.3 Compatibility with SKA1-MID band 2 survey

We further discuss to what extent the proposed SKA1-MID band 2 reference survey (Sect. 2.4) can satisfy studies related to the RC emission from the ISM in selected galaxies. As the observed emission is the sum of the thermal and nonthermal components, the mean signal-to-noise ratio at the observer-frame is given by $\langle S/N \rangle = \langle I_{\nu_2}^{\text{tot}} \rangle / N$, with $\langle I_{\nu_2}^{\text{tot}} \rangle = \langle I_{\nu_2}^{\text{th}} \rangle + \langle I_{\nu_2}^{\text{nt}} \rangle$ and N the sensitivity or the one σ rms noise level of the survey. The mean signal-to-noise ratios obtained for the 3 tiers of UDT, DT, and WT are plotted against redshift (Fig. 7) and the corresponding values at selected redshifts of 0.15, 0.3, 0.5, 1, 2 are listed in Tables 2 and 3. Generally, the signal-to-noise ratios decrease with redshift in case(1), while they increase in case(2) as expected from the redshift evolution of the mean surface brightnesses (Sect. 3.1).

From $z = 0$ out to $z = 3$, UDT can detect the mean RC emitting ISM above 8σ and 4σ levels in galaxies like M51 and NGC6946, respectively, in case (1). In M33-like galaxies, $\langle S/N_{\text{UDT}} \rangle \gtrsim 3$ occurs only at $z \lesssim 0.3$. DT can detect the mean ISM of the M51-like galaxies at $> 3\sigma$ while a 3σ detection is only possible up to $z = 0.6 - 0.7$ for NGC6946-like galaxies. WT detects none of these galaxies at 3σ level in case of no evolution in radio size.

Based on the case (2) results, the mean RC emitting ISM is detected in all galaxies above the 4σ level in UDT at all redshifts. However, only M51- and NGC6946-like galaxies are detected in DT with $\langle S/N_{\text{DT}} \rangle \geq 8$. Such a detection is only possible for M51-like galaxies at $z \gtrsim 1$ in WT.

According to Prandoni & Seymour (2015), the scope of the three-tiered surveys was to study galaxies at different SFR levels at different redshifts (their Table 2). Specifically, UDT was designed to probe $\text{SFR} \sim 10$ galaxies at $z \sim 3 - 4$, DT to study $\text{SFR} \sim 10$ galaxies at $z \sim 1 - 2$, and WT for detecting galaxies with $0.5 < \text{SFR} < 10$ at $0 < z < 1$. As these SFR levels are similar to those of our sample at corresponding redshifts (see Table 1), we further discuss the extent to which the above scopes can be met. The ultimate goal of the UDT survey is to study M33-like galaxies (with $\text{SFR} \sim 10$ at $z \sim 3 - 4$) which can be achieved only in case (2). Similarly, the DT goal can be reached only in case (2), as the $\text{SFR} \sim 10$ galaxies at $z \sim 1 - 2$ are like NGC 6946 which are below 3σ detection limit in case (1) at those redshifts. The WT goal is met only for M 51-like galaxies at $z \lesssim 0.3$ in case (2). At higher redshifts ($0.3 < z < 1$), galaxies have SFRs similar to M 33 and NGC 6946 ($0.5 < \text{SFR} < 10$) which are undetected in both cases (1) and (2). It is hence important to reconsider the Band 2 three tiered surveys particularly if there is no radio-size evolution.

4.3.1 Detecting galactic structures

Moving from $z = 1$ to $z = 0.15$, galactic structures such as clumps in disks, spiral arms, and star-forming associations are potentially observable at $0.6''$ angular resolution (see Figs. 2 to 4). The spiral arms can be resolved at scales of ≤ 1 kpc at $z = 0.15$ for both cases (1 and 2). At $z = 0.3$, the spiral arms can still be distinguished in case (1), while only a clumpy disk appears in case (2). Detecting structures is limited to spatial scales of few kpc at $z \geq 1$ in both cases (1) and (2). Hence, studies of the inner vs. outer disks as well as structures at larger spatial scales in the intergalactic medium are

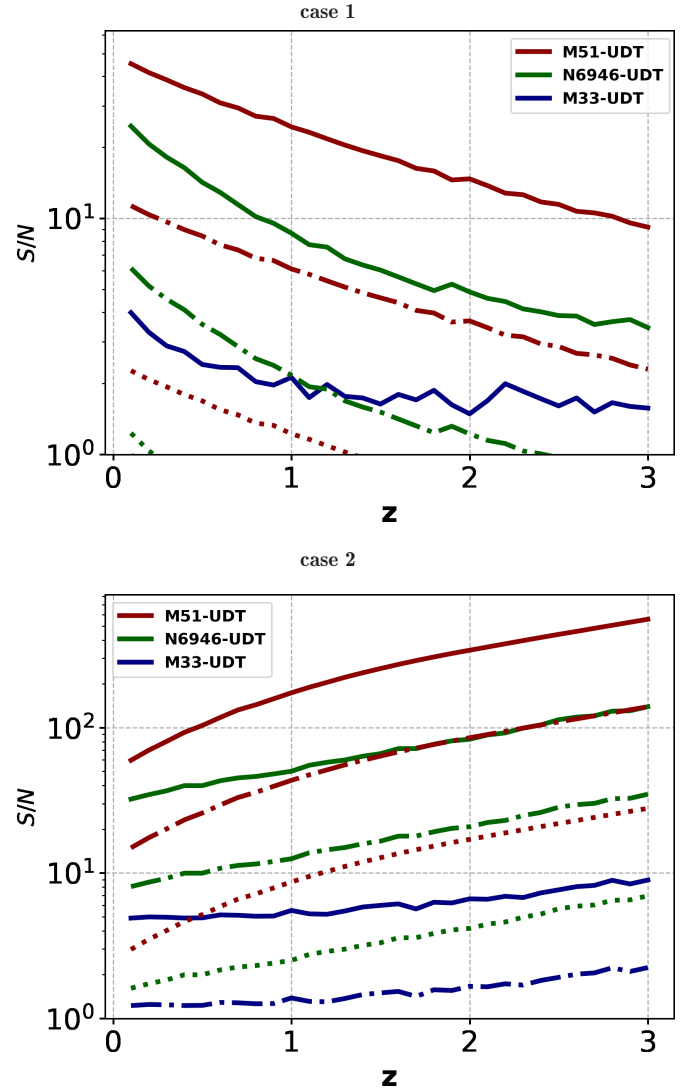


Figure 7. The mean signal to noise ratio $\langle S/N \rangle$ based on the SKA1-MID band 2 UDT (solid), DT (dashed-dotted), and WT (dotted) for case 1 (top) and case 2 (bottom) at the observed frequency of 1.4 GHz (equivalent to a rest-frame frequency of 1.6–5.6 GHz at $0.15 \leq z \leq 3$).

in principle feasible. To assess the capability of the SKA1-MID band 2 survey in detecting these structures, we derive the maps of signal-to-noise ratio ($S/N = I_{\nu_2}^{\text{tot}}/N$) by dividing the sum of the thermal and nonthermal maps simulated by the sensitivities of the three-tiered survey given in Sect. 2.4. These maps are shown in Fig. 8 at the selected redshifts of $z = 0.15, 0.3, 0.5, 1$, and 2 for UDT. The structures detected in the three tiers are:

- M51-like galaxies: In case (1), all structures described in Sect. 3.2 can be detected above 10σ at all redshifts in UDT, but the outer disk is not detected at $z \gtrsim 2$ in DT and at $z > 0.3$ in WT. In the latter tier, only the very central part is detected at $z > 1$. In case (2), all structures are detected in all three tiers.
- N6946-like galaxies: The disk is visible at $S/N > 5$ and 50 in case (1) and (2), respectively, in UDT. DT cannot detect

the entire disk at $z = 1$ and only the inner disk can be studied at $z = 2$ for case (1). This tier can detect all structures in case(2). WT can hardly detect the entire disk at $z \gtrsim 0.3$ in case (2). It may only detect the central part at $0.3 \lesssim z \lesssim 1$ in case(1).

- M33-like galaxies: In UDT, the diffuse emission from the outer disk, spiral arms and star-forming regions can all be detected ($S/N > 3$) up to $z=0.15$ in case (1). The sensitivity to detect the outer disk is reduced for $z \geq 0.3$. The disk is undetected for $z = 1$ and higher. DT and WT cannot detect these galaxies. In case (2), i.e., if radio sizes evolve with z , almost all structures can be observed at all redshifts in UDT, but only the central disk up to $z = 0.3$ in DT and no detection in WT.

It is worth noting that the size evolution of galaxies such as that considered in case (2) is established based on the rest-frame ultraviolet and optical observations by HST (e.g., Ferguson et al. 2004; Mosleh et al. 2011; Ono et al. 2013; van der Wel et al. 2014; Shibuya et al. 2015). However, radio observations provide no clear consensus on the size evolution (e.g., Murphy et al. 2017; Guidetti et al. 2017; Cotton et al. 2018; Bondi et al. 2018). One reason can be a possible dilution by the presence of radio AGNs (Bondi et al. 2018). Another reason is the different spatial scales on which synchrotron emission occurs at different frequencies. Assuming that the size evolution is shallower at longer wavelengths (e.g., van der Wel et al. 2014) and that the case (2) evolution is more justified for a rest-frame optical emission, our simulation of the thermal radio emission traced using the $H\alpha$ emission is best represented through this case, and the nonthermal emission by an evolution that is closer to case (1). Hence, the galaxy size evolution observed in the radio (sum of the thermal and nonthermal emission) might occur in between the cases (1) and (2) as extreme scenario. This agrees with Jiménez-Andrade et al. (2019) finding a shallow evolution of $r_e \sim (1+z)^{(-0.26 \pm 0.08)}$ for the radio continuum size evolution of star-forming galaxies over the redshift range $0.35 < z < 2.25$ using the VLA COSMOS 3GHz survey.

4.4 Comparisons with the literature studies

Observational studies are mostly limited to integrated properties up to now. Therefore, we discuss and compare the integrated flux densities, S_{ν_2} , with those in the literature. This should be instructive for unresolved studies in general. The evolution in S_{ν_2} given by Eq. 5 is similar to that of the surface brightness I_{ν_2} in case (1) (Eq. 9). We are witnessing a drop in both the thermal and the nonthermal RC flux densities¹³, $S_{\nu_2}^{\text{th}}$ and $S_{\nu_2}^{\text{nt}}$, with z similar to what is shown in the two upper left panels in Fig. 1 at $\nu_2 = 1.4$ GHz (equivalent to 1.6–5.6 GHz rest-frame frequencies at $0.15 \leq z \leq 3$). As explained in Sect. 3.1, the global evolution is uncertain for M33-like galaxies and, hence, here we compare the evolutionary trends for other galaxy types only. From $z = 0.15$ to $z = 2$, $S_{\nu_2}^{\text{nt}}$ decreases by a factor of $\simeq 3$ and 4.5 in M51- and NGC6946-like galaxies, respectively. At the same redshift range, $S_{\nu_2}^{\text{th}}$ drops by a factor of $\simeq 1.6$ and 2 for M51- and NGC6946-like galaxies, respectively (see Table 2). Thus, the

rate of this drop is faster for lower mass galaxies in general. As a matter of fact, a mass dependency is expected through the evolution of SFR (Eq. 1). It is also interesting to note that the nonthermal emission drops faster than the thermal emission. This is caused by the nonthermal emission dropping faster with increasing frequency (we remind that the rest-frame frequency probed increases with redshift). This effect can reduce the detection chance of high- z normal star-forming galaxies at observed frequencies higher than the mid-radio frequencies studied here. Such a deficit in the nonthermal emission at high frequencies can also lead to an underestimation of the radio-based SFR at high-redshifts as noted by Algera et al. (2021) studying a sample of galaxies in the COSMOS and GOODS-North fields at the rest-frame frequencies $\simeq 65$ -90 GHz.

In the MIGHTEE-COSMOS field, An et al. (2021) found that the ratio of the observed total flux densities observed at 1.3 GHz-to-3 GHz increases very slowly with stellar mass, though with a large scatter. Neglecting thermal contamination, this was explained by synchrotron losses in more massive galaxies. Here, we find a steeper 1-10 GHz synchrotron spectrum for the most massive, M51-like galaxies compared to the others only for $z < 0.5$. We also caution that, although more massive galaxies are expected to have a larger magnetic field strength (Tabatabaei et al. 2016), the cooling of cosmic ray electrons does not depend only on the magnetic field strength in galaxies (e.g., Longair 1994). Moreover, the structure of the magnetic field can also play a role: A more tangled field increases the chance of scattering and decoupling of high-energy particles from the magnetic field (e.g., Tabatabaei et al. 2017). This can explain the faster drop of α_{nt} vs. z in M51-like galaxies than in others due to a faster increase of SFR activities, following Eq. 1, inducing more turbulent/tangled fields at high z . The result obtained by An et al. (2021) will be revisited after separating the thermal/nonthermal emission for the MIGHTEE-COSMOS galaxies (Tabatabaei et al in prep.).

5 SUMMARY

The thermal and nonthermal components of the radio continuum (RC) emission are ideal tracers of energetic processes in galaxies, hence, studying them over cosmic time can shed light on the evolution of galaxies. This paper presents a study of the cosmic evolution of the thermal and nonthermal RC emission from normal star-forming galaxies by simulating the RC emission properties of present-day galaxies at earlier cosmic epoch between $0.15 < z < 3$. The goals are to investigate 1) the expected structure of thermal and nonthermal emission on $\gtrsim 1$ kpc scales at different redshifts, 2) a possible evolution of the thermal fraction and synchrotron spectral index at mid-radio frequencies (1-10 GHz), and 3) the potential of the upcoming SKA1-MID reference surveys to detect RC emitting structures that are needed to address the role of thermal/nonthermal processes in the evolution of galaxies. Surface brightness maps are created at the observed frequency of 1.4 GHz at an angular resolution of $0.6''$ considering two different scenarios: 1) no galaxy size evolution in the radio and 2) that radio sizes evolve with redshift similarly to optical size variation. The most important findings are summarized as follows:

¹³ However, we note that their corresponding luminosity increases with z following the expected increase in SFR.

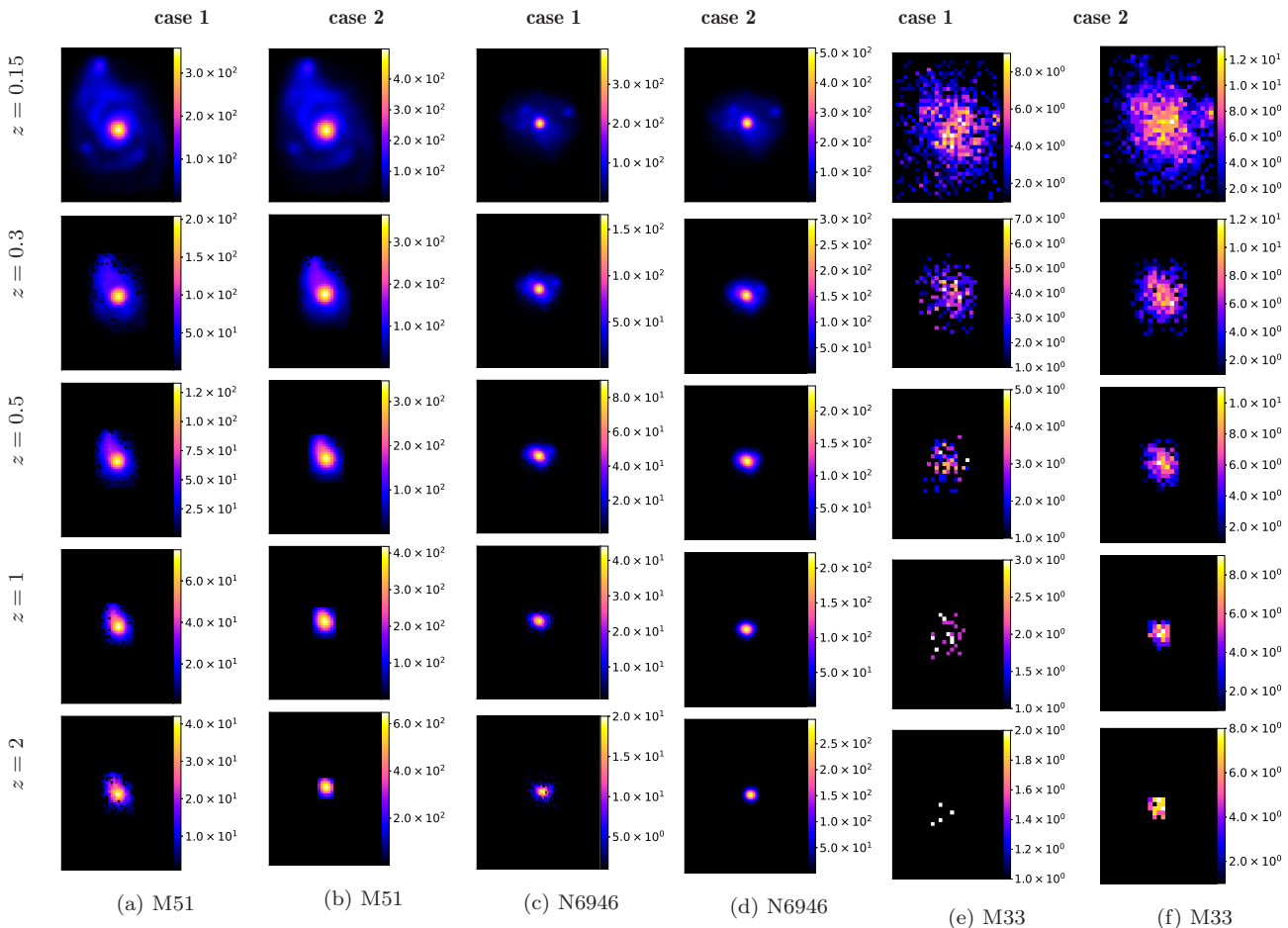


Figure 8. The signal-to-noise ratio S/N maps for a M51-like galaxy for case 1 (*first column*), case 2 (*second column*), NGC6946-like galaxy for case 1 (*third column*), case 2 (*fourth column*) and M33-like galaxy for case 1 (*fifth column*), case 2 (*sixth column*) based on the SKA1-MID band 2 UDT survey at the observed frequency of 1.4 GHz. From top to bottom: $z = 0.15, 0.3, 0.5, 1,$ and 2 .

- **General trends:** The mean thermal and nonthermal surface brightnesses drop with z in case (1) but they increase in case (2) because, at higher z , galaxy sizes become smaller. As a result of the size shrinking, the structures simulated are less resolved in the case (2) than in case (1). We note that the information about the diffuse emission (spatial extent) from the outer disks is more redshift-dependent in the case (1).

- **Evolution of the thermal fraction:** As the synchrotron emission drops faster than the free-free emission at higher frequencies (due to the spectral dependencies, $\alpha_{\text{nt}} > \alpha_{\text{th}}$), the mean thermal fraction observed at 1.4 GHz increases with redshift (by $\gtrsim 30\%$ from $z = 0.15$ to $z = 2$) in case (1). The trend is, however, more complex in case (2) as the surface brightness enhancement with z is dominated by that of the nonthermal emission. This leads to a turnover in $\langle f_{\nu_2}^{\text{th}} \rangle(z)$ at $z \simeq 1$. In lower mass galaxies, the thermal fraction is generally higher than in higher mass galaxies.

- **Evolution of the nonthermal spectrum:** We predict that the mid-radio (1-10 GHz) nonthermal spectrum flattens with increasing redshift: α_{nt} drops from 0.8-0.9 to 0.5-0.6 in case (1) and even more for case (2) moving back in time from $z = 0$ to $z = 2$, indicating that cosmic ray electrons used to be more energetic due to higher star formation activities. Current observations match better with the case (1) than the case (2) predictions. In more massive galaxies like

M51, the spectral index evolves faster with z , and α_{nt} is steeper than in other galaxies only at $z < 0.5$. The flattening of α_{nt} , causes a curvature in the observed mid-radio SED of galaxies at higher z .

- **Progress with SKA:** Assuming that galaxy sizes evolve little in the radio - as suggested by our comparison of case (1) predictions and observational data, as well as recent literature (Jiménez-Andrade et al. 2019) - the SKA1-MID band 2 survey can detect ISM structures in M51- and NGC6946-like galaxies at all redshifts studied here ($z \leq 3$) in UDT. Depending on redshift, the disk of galaxies can still be partly detected with the two other tiers, DT and WT. The mean RC emission from low-mass galaxies like M33 can only be detected at 3σ level up to $z = 0.5$ in UDT. These findings show that the scientific goals defined for the SKA1-MID band 2 surveys cannot be fully met if the radio-size of galaxies remains fixed with redshift. At the selected resolution of $0.6''$, spiral arms can be distinguished out to $z < 1$. These can be in principle detected at higher z with SKA adopting higher angular resolutions but at a lower S/N.

Last but not the least, constraining the mid-radio SED of galaxies is fundamental to separating the thermal and non-thermal emissions and calibrating SFR (Tabatabaei et al. 2017) independently from the RC-IR correlation at high z .

However, complete sampling of the mid-radio SED will be possible only up to $z = 1$ with the currently proposed SKA1-MID surveys (see Sect. 2.4). To address the evolution of galaxies, studies of the epoch of maximum star formation (i.e., $z \simeq 2$) are crucial. This study suggests that band 1 must be included in the SKA1-MID surveys to constrain the mid-radio SED of galaxies at this epoch. This will further help to disentangle AGN/starburst candidates and to understand the evolution of the radio–infrared correlation in galaxies.

ACKNOWLEDGEMENTS

The authors thank Robert Braun and the SKA organization team for their help and useful discussions. We also thank the anonymous referee for his/her helpful comments. MG-N acknowledges support from Iran’s National Elites Foundation (INEF). MTS acknowledges support from a Scientific Exchanges visitor fellowship (IZSEZO_202357) from the Swiss National Science Foundation.

Data Availability

The simulated data will be made available on [figshare](https://figshare.com).

REFERENCES

- Algera H. S. B., et al., 2021, ApJ (in press), arXiv:2111.01153
 An F., et al. 2021, MNRAS, 507, 2643
 Appleton P. N., et al. 2004, ApJS, 154, 147
 Basu A., et al. 2015, ApJ, 803, 51
 Beck R., 1991, A&A, 251, 15
 Beck R., 2007, A&A, 470, 539
 Bell, E. F. 2003, ApJ, 586, 794
 Berkhuijsen E. M., Beck R., Tabatabaei F. S., 2013, MNRAS, 435, 1598.
 Bisigello, L., et al., 2018, A&A, 609, A82
 Bonato, M., et al., 2017, MNRAS, 469, 1912
 Bondi, M. et al. 2018, A&A, 618, L8
 Bourne, N., Dunne, L., Ivison, R. J., et al. 2011, MNRAS, 410, 1155
 Braun R., Bonaldi A., Bourke T., Keane E., Wagg J., 2019, arXiv:1912.12699
 Brownson S., et al. 2020, MNRAS Letters, 498, L66
 Cecil G., 1988, ApJ, 329, 38.
 Cedrés B., Cepa J., Bongiovanni Á., Castañeda H., Sánchez-Portal M., Tomita A., 2013, A&A, 560, A59.
 Chyży K. T., Weżgowiec M., Beck R., Bomans D. J., 2011, A&A, 529, A94
 Ciardullo, R., et al. 2002, ApJ, 577, 31
 Condon, J., J.1984, ApJ, 287, 461
 Condon, J. J., et al., 2002, AJ, 124, 675
 Corbelli E., 2004, NewAR, 48, 1275.
 Cotton, W. D., Condon, J. J., Kellermann, K. I., et al. 2018, ApJ, 856, 67
 Daddi E., et al. 2010, ApJL, 714, L118
 Delhaize J., et al., 2017, A&A, 602, A4
 Delvecchio I., et al., 2017, A&A, 647, 123
 Driver S. P., et al., 2013, MNRAS, 430, 2622
 Dumas G., et al., 2011, AJ, 141, 41
 Ferguson, H. C., Dickinson, M., Giavalisco, M., et al. 2004, ApJ, 600, L107
 Fletcher A., et al. 2011, MNRAS, 412, 2396
 Freedman, W. L., et al. 1991, ApJ, 372, 455
 Garrett, M. A. 2002, A&A, 384, L19
 Gatto A., et al., 2017, MNRAS, 466, 1903
 Gran T., et al., 2009, MNRAS, 397, 1101
 Greve T. R., et al., 2005, MNRAS, 359, 1165
 Grϕnnow A., et al., 2022, MNRAS, 509, 5756
 Guidetti, D., Bondi, M., Prandoni, I., et al. 2017, MNRAS, 471, 210
 Hassani et al. 2021, MNRAS, in press, arXiv:2111.00583
 Heesen V., et al., 2014, AJ, 147, 130
 Horellou C., et al., 1992, A&A, 265, 417
 Hubble, E., Tolman, R. C. 1935, ApJ, 82, 302
 Hunt Q., et al. 2018, ApJL, 820, L18
 Huynh, M. T., Frayer, D. T., Mobasher, B., et al. 2007, ApJ, 667, L9
 Ishwar-Chandra, C. H., 2010, MNRAS, 405, 436
 Ivison, R. J., Alexander, D. M., Biggs, A. D., et al. 2010, MNRAS, 402, 245
 Jiménez-Andrade, E. F., Magnelli, B., Karim, A., et al. 2019, A&A, 625, 114
 Karachentsev, I. D., et al., 2000, A&A, 362, 544
 Karachentsev et al. 2013
 Kennicutt R. C., et al., 2011, PASP, 123, 1347
 Klein et al., 1984, A&A, 135, 213
 Kroupa P., 2002, Sci, 295, 82.
 Lacki et al., 2010, ApJ, 717, 1
 Leroy et al. 2008, ApJ, 136, 2782
 Leslie, Sarah K.; Schinnerer, Eva; Liu, Daizhong et al., 2020ApJ, 899, 58
 Lee N., et al., 2015, ApJ, 801, 80
 Longair M. S., High energy astrophysics. Vol.2: Stars, the galaxy and the interstellar medium, Cambridge University Press
 Mathews W. G., 2009, ApJL, 695, 1, L49
 Madau P., Dickinson M., 2014, ARA&A, 52, 415
 Magnalli B., et al. 2015, A&A, 573, 45
 Molnar et al., 2021, MNRAS, 504, 118
 Mosleh, M., William, R. J., et al., 2011, ApJ, 727, 5
 Mueller, O., & Jerjen, H., 2020, A&A, 644, 91
 Mulcahy D. D., et al., 2018, 615, 98
 Murphy E. J., et al., 2011, ApJ, 737, 67
 Murphy E. J., 2013, ApJ, 777, 58
 Murphy E. J., et al., 2015, Advancing Astrophysics with the Square Kilometre Array (AASKA14), p. 85
 Murphy, E. J., Momjian, E., Condon, J. J., et al. 2017, ApJ, 839, 35
 Neininger N. & Horellou C., 1996, ASPC, 97, 592
 Niklas S., Beck R., 1997, A&A, 320, 54
 Noeske K. G., et al., 2007, ApJL, 660, L43
 Norris, Ray P.; Huynh, Minh T.; Jackson, Carole A., et al., 2005, AJ, 130, 1358
 Ono, Y., Ouchi, M., Curtis-Lake, E., et al. 2013, ApJ, 777, 155
 Owen, E. R., et al. 2019, A&A, 626, 85
 Peng Y., et al., 2015, Nature, 521, 192
 Pillai, T, et al., 2015, ApJ, 799, 74
 Pfrommer C., Pakmor R., Schaaf K., Simpson C. M., Springel V., 2017, MNRAS, 465, 4500. doi:10.1093/mnras/stw2941
 Prandoni, I., Seymour, N., 2015, SKA Book 'Advancing Astrophysics with the SKA' (AASKA14) - Continuum Science', p67, arXiv:1412.6942
 Planck Collaboration, et al., 2018, arXiv, arXiv:1807.06209
 Querejeta M., Schinnerer E., García-Burillo S., Bigiel F., Blanc G. A., Colombo D., Hughes A., et al., 2016, A&A, 593, A118.
 Read S.C., et al. 2018, MNRAS, 480, 5625
 Richards, E. A., Kellermann, K. I., Fomalont, E. B., et al. 1998, AJ, 116, 1039
 Roettgering, H. J. A., et al. 1994, A&AS, 108, 79
 Sajina, A., et al. 2008, ApJ, 683, 659
 Samui, S., et al. 2018, MNRAS, 476, 1680-1695
 Sargent, M. T. et al., 2010, ApJ, 186, 341
 Schaye J., et al., 2015, MNRAS, 446, 521

- Schreiber C., et al., 2015, *A&A*, 575, A74
 Scoville, N., & Young, J. S., 1983, *ApJ*, 265, 148
 Scoville N., et al., 2016, *ApJ*, 820, 83
 Scoville N., et al., 2017, *ApJ*, 837, 150
 Seymour, N., et al., 2008, *MNRAS*, 386, 1695
 Shao, S., et al. 2018, *MNRAS*, 479, 284
 Shibuya, T., Ouchi, M., & Harikane, Y. 2015, *ApJS*, 219, 15
 Singh V., et al. 2014, *A&A*, 569, 52
 Speagle J. S., Steinhardt C. L., Capak P. L., Silverman J. D., 2014, *ApJS*, 214, 15
 Suess K. A., Kriek M., Price S. H., Barro G., 2019, *ApJ*, 877, 103. doi:10.3847/1538-4357/ab1bda
 Straatman, C. M. S., Labbe, I., Spitler, L. R., et al. 2015, *ApJ*, 808, L29
 Tabatabaei F. S., et al., 2007 *A&A*, 472, 785
 Tabatabaei F. S., et al., 2007, *A&A*, 475, 133
 Tabatabaei, F. S., Krause, M., Fletcher, A., & Beck, R. 2008, *A&A*, 490, 1005
 Tabatabaei F. S., et al., 2013, *A&A*, 552, 19
 Tabatabaei F. S., et al., 2013, *A&A*, 557, 129
 Tabatabaei F. S., et al., 2016, *ApJ Letters*, 818L, 10
 Tabatabaei F. S., et al., 2017, *ApJ*, 836, 185
 Tabatabaei F. S., et al., 2018, *Nature Astronomy*, 2, 83
 Tacconi L. J., et al., 2013, *ApJ*, 768, 74
 Tacconi L. J., et al., 2018, *ApJ*, 853, 179
 Tisanić K., Smolčić V., Delhaize, et al., 2019, *A&A*, 621, 139
 Tolman, R. C., *Proc. Natl. Acad. Sci.*, 16, 511
 Tolman, R. C., *Relativity, Thermodynamics and Cosmology* (Oxford: Oxford Univ. Press)
 Tomczak A. R., et al., 2016, *ApJ*, 817, 118
 van der Wel, A., Franx, M., van Dokkum, P. G., et al. 2014, *ApJ*, 788, 28
 Verley S., Corbelli E., Giovanardi C., Hunt L. K., 2009, *A&A*, 493, 453
 Walter F., et al., 2016, *ApJ*, 833, 67
 Walter F., et al., 2020, *ApJ*, 902, 111
 Westcott et al., 2018, *MNRAS*, 475, 5116
 Whitaker et al., 2014, *ApJ*, 795, 104
 Zovaro H. R. M. et al., 2022, *MNRAS*, 509, 4997

APPENDIX

THERMAL/NON-THERMAL SEPARATION METHOD

The thermal and nonthermal components of the radio continuum emission are mapped using the TRT method developed by Tabatabaei et al. (2007b) and Tabatabaei et al. (2013a) in which a de-reddened H α map is used to trace the thermal free-free emission in galaxies. As the thermal radio emission is expected to arise generally from ionized media irrespective from their ionization sources, a physically motivated thermal tracer should map the thermal radio emission from not only star-forming regions but also diffuse ionized gas in galaxies. Recombination lines, with the H α line being the brightest one, can ideally do the job as a physical balance is expected between ionization and recombination rates in an ionized gas.

At frequency ν , the relation between the thermal free-free brightness temperature T_b in Kelvin (K) and the H α surface brightness $I_{H\alpha}$ in $\text{erg cm}^{-2} \text{s}^{-1} \text{sr}^{-1}$ is given by

$$\begin{cases} T_b = T_e(1 - e^{-A I_{H\alpha}}), \\ A = 3.763 \nu_{GHz}^{-2.1} T_e^{-0.3} 10^{\frac{0.029}{T_e^4}}, \end{cases} \quad (1)$$

where T_e is the electron temperature in K and $T_{e4} = T_e/10^4 K$. In the above relation, the contribution from singly

ionized He is also taken into account. The thermal free-free surface brightness I^{th} in mJy/beam is then obtained using

$$I_\nu^{\text{th}} = \frac{\theta_i \theta_j}{1224} \nu_{GHz}^2 T_b, \quad (2)$$

with θ_i and θ_j the beam width along the major and minor axes in arcsec. Subtracting this emission from the observed surface brightness I^{obs} , the nonthermal surface brightness is obtained $I_\nu^{\text{nt}} = I_\nu^{\text{obs}} - I_\nu^{\text{th}}$.

To de-reddening the H α map, different techniques are used depending on the available data. Ideally, the ratio of two recombination lines can be used to correct the effect of dust extinction (Tabatabaei et al. 2018). Using dust mass maps also provide an efficient information thanks to Spitzer and Herschel infrared maps of nearby galaxies (e.g. Hassani et al. 2021).

This paper has been typeset from a $\text{T}_\text{E}\text{X}/\text{L}^\text{A}\text{T}_\text{E}\text{X}$ file prepared by the author.